



# Rational design and synthesis of SnO<sub>2</sub>-encapsulated $\alpha$ -Fe<sub>2</sub>O<sub>3</sub> nanocubes as a robust and stable photo-Fenton catalyst

Na Wang, Yunchen Du\*, Wenjie Ma, Ping Xu, Xijiang Han\*

MIIT Key Laboratory of Critical Materials Technology for New Energy Conversion and Storage, School of Chemistry and Chemical Engineering, Harbin Institute of Technology, Harbin 150001, China

## ARTICLE INFO

### Article history:

Received 5 December 2016

Received in revised form 7 March 2017

Accepted 12 March 2017

Available online 15 March 2017

### Keywords:

Fe<sub>2</sub>O<sub>3</sub>@SnO<sub>2</sub> nanocubes

Prussian blue

Phase transformation

RhB degradation

Photo-Fenton reaction

## ABSTRACT

*In situ* transformation of metal-organic frameworks (MOFs) is becoming a fascinating strategy to construct porous metal oxides with excellent performance in many fields. In this work, Prussian blue (PB) nanocubes are employed as the precursor of porous Fe<sub>2</sub>O<sub>3</sub> to fabricate SnO<sub>2</sub>-encapsulated  $\alpha$ -Fe<sub>2</sub>O<sub>3</sub> (Fe<sub>2</sub>O<sub>3</sub>@SnO<sub>2</sub>) nanocubes by pre-coating Sn(OH)Cl on the surface of PB nanocubes. It is very interesting to find that SnO<sub>2</sub> shells can not only preserve the microstructure of Fe<sub>2</sub>O<sub>3</sub> nanocubes from high-temperature treatment, but also facilitate the phase variation from metastable  $\gamma/\beta$ -phase to stable  $\alpha$ -phase. The thickness of SnO<sub>2</sub> shells can be controlled by manipulating the amount of stannous chloride. When Fe<sub>2</sub>O<sub>3</sub>@SnO<sub>2</sub> nanocubes are applied as heterogeneous photo-Fenton catalysts, they will exhibit much better catalytic efficiency for the degradation of Rhodamine B (RhB) than PB-derived Fe<sub>2</sub>O<sub>3</sub> and commercial  $\alpha$ -Fe<sub>2</sub>O<sub>3</sub>. The characterization results reveal that Fe<sub>2</sub>O<sub>3</sub>@SnO<sub>2</sub> nanocubes have similar catalytic mechanism to conventional  $\alpha$ -Fe<sub>2</sub>O<sub>3</sub>, and stable microstructure and preferable crystalline phase are primarily responsible for this significant enhancement. Some influential factors, including H<sub>2</sub>O<sub>2</sub> concentration, catalyst dosage, pH value, and reaction temperature are investigated and analyzed in details. Moreover, Fe<sub>2</sub>O<sub>3</sub>@SnO<sub>2</sub> nanocubes can maintain their catalytic efficiency during the repeated batch experiments. We believe Fe<sub>2</sub>O<sub>3</sub>@SnO<sub>2</sub> nanocubes can be a new kind of high-performance green heterogeneous catalyst for the degradation of organic pollutants, and this study may provide a new idea to upgrade the performance of some conventional catalysts by rational design in the future.

© 2017 Elsevier B.V. All rights reserved.

## 1. Introduction

Water scarcity has been listed as one of the three global systemic risks of highest concern, which not only came from declining groundwater tables, reduced river flows, shrinking lakes, but also resulted from the heavy pollution of wastewater discharge in the flourishing urbanization and industrialization [1,2]. It is a preferable way to alleviate the water crisis by technologically purifying the wastewater in terms of pollutants removal and disinfection of bacteria into clean water to guarantee the water security issue [3]. During the past decades, some conventional physical, chemical and biological technologies played a significant role in wastewater treatment and environmental remediation [4–6], however, their effectiveness for the removal of recalcitrant organic contaminants such as dyes, phenols, halogenides, nitro-compounds, was still lim-

ited [7–9]. As a well-known case of advanced oxidation processes (AOPs) [10–12], Fenton chemistry combined with light irradiation, based on high reactivity and non-selectivity of hydroxyl radical (HO<sup>•</sup>), has become a kind of powerful and high-efficiency oxidation technology that could greatly promote the decomposition of toxic and persistent organic contaminants in wastewater [13–16].

In view of the unique advantages in separation and regeneration, there are numerous interests in developing high-performance heterogeneous catalysts for activating H<sub>2</sub>O<sub>2</sub> in Fenton system, where hematite ( $\alpha$ -Fe<sub>2</sub>O<sub>3</sub>) is believed to be a promising candidate due to its low cost, simple chemical composition, stable structure and environmental benignity [17–20]. It is well known that the large surface area and high porosity of heterogeneous catalyst generally make considerable contribution to the catalytic efficiency, and thus rationally design and preparation of porous  $\alpha$ -Fe<sub>2</sub>O<sub>3</sub> by soft-template and hard-template methods have attracted widespread attention [21–24]. For example, Wang and co-workers synthesized hollow  $\alpha$ -Fe<sub>2</sub>O<sub>3</sub> spheres with sheet-like subunits via an interesting glycerol/water quasiemulsion-templating method [23]. Jiao et al. employed KIT-6 as a hard template to manipulate a near-single

\* Corresponding authors.

E-mail addresses: [yunchendu@hit.edu.cn](mailto:yunchendu@hit.edu.cn) (Y. Du), [\(X. Han\).](mailto:hanxijiang@hit.edu.cn)



crystal-like  $\alpha$ -Fe<sub>2</sub>O<sub>3</sub> with highly ordered mesoporous structure [24]. However, either soft-template method or hard-template method is generally restricted by the complicated procedures and rigorous conditions, especially the hydrolysis of iron salts should be precisely controlled.

Recently, *in situ* transformation of metal-organic frameworks (MOFs) appears as a very attractive strategy for the preparation of metal oxides, where MOFs can act as a self-sacrificing template and porous structure may be constructed during the decomposition of organic ligands [25–31]. The as-prepared metal oxides in this way usually display significant improvements in different applications as compared with their conventional counterparts. For instance, Lv et al. fabricated highly porous Co<sub>3</sub>O<sub>4</sub> concave cubic particles by the calcination of Co-based metal-organic framework (ZIF-67), where the extremely high specific surface area was confirmed to be favorable for its outstanding performance in gas sensing application [25]; Zhang et al. demonstrated the synthesis of hollow CuO/Cu<sub>2</sub>O octahedrons by annealing [Cu<sub>3</sub>(btc)<sub>2</sub>]<sub>n</sub>, (btc = benzene-1,3,5-tricarboxylate), and the obtained composites displayed cycling stability and good rate capability as novel anode materials for sodium ion batteries [26]; Chen et al. designed multivariate mixed-metal oxides (Ni<sub>x</sub>Co<sub>3-x</sub>O<sub>4</sub>) with a high surface area using bimetallic MOF-74-NiCo as a precursor, which showed obvious advantages as electrode materials for supercapacitors [27]. As a typical Fe-MOFs, Prussian blue (PB) with composition of Fe<sub>4</sub>[Fe(CN)<sub>6</sub>]<sub>3</sub> was also applied for the synthesis of porous Fe<sub>2</sub>O<sub>3</sub> nanocubes by a simple annealing treatment [32,33]. However, it was found that the resultant Fe<sub>2</sub>O<sub>3</sub> nanocubes were consisted of mixed  $\beta$ - and  $\gamma$ -phases. Compared with the desirable  $\alpha$ -Fe<sub>2</sub>O<sub>3</sub>,  $\beta$ - and  $\gamma$ -Fe<sub>2</sub>O<sub>3</sub> are metastable, and their catalytic efficiencies in photo-Fenton systems are usually inferior [34,35]. Although the high-temperature treatment is considered to be an effective route to realize the phase transformation from  $\gamma/\beta$ -Fe<sub>2</sub>O<sub>3</sub> to  $\alpha$ -Fe<sub>2</sub>O<sub>3</sub>, irreversible collapse of the microstructure induced by hyperthermia will certainly lead to negative impact on the catalytic activity [36,37]. Therefore, it will be a challenging task to induce the phase transformation of PB-derived Fe<sub>2</sub>O<sub>3</sub> nanocubes from  $\beta$ -/ $\gamma$ -phases to  $\alpha$ -phase on the premise of stabilizing their microstructure.

In addition to the optimization of microstructure and crystalline phase, constructing Fe<sub>2</sub>O<sub>3</sub>-based nanocomposites offers an alternative to enhance the catalytic activity of Fe<sub>2</sub>O<sub>3</sub>. Among various candidates, SnO<sub>2</sub>, a wide-energy-gap semiconductor (3.6 eV), usually emerges as a popular secondary component, because the synergistic effect derived from the heterojunction structure between Fe<sub>2</sub>O<sub>3</sub> and SnO<sub>2</sub> are greatly helpful to extend the light absorption range and reduce the recombination of photo-generated electrons and holes [18,38–40]. In order to take full advantage of the heterojunction structure, some groups even gave more elaborations on the fabrication of SnO<sub>2</sub>/Fe<sub>2</sub>O<sub>3</sub> composites. For instance, Kang et al. presented a novel necklace like SnO<sub>2</sub>/ $\alpha$ -Fe<sub>2</sub>O<sub>3</sub> heterostructure by chemical vapor deposition method in which Fe<sub>2</sub>O<sub>3</sub> hexagonal disks hierarchically grew on a nanocable with SnO<sub>2</sub> nanowire as core and Fe<sub>2</sub>O<sub>3</sub> epitaxial layer as shell [41]; Mi et al. directed the secondary growth of SnO<sub>2</sub> nanorods on the external surface of  $\alpha$ -Fe<sub>2</sub>O<sub>3</sub> nanotubes/nanorings to produce larger heterostructure interface [42]. Although these successful examples have made significant achievements, most of them just focused on the synergistic effect between Fe<sub>2</sub>O<sub>3</sub> and SnO<sub>2</sub> without paying any attention to some versatile functions of SnO<sub>2</sub> in other aspects. In the recent advances of core/shell inorganic composites, tin oxide (SnO<sub>2</sub>) is also being regarded as a promising shell candidate that can prevent the agglomeration of monodispersed nanoparticles or stabilize the microstructure of composites [43–45]. What's more, some researches demonstrated that the presence of Sn<sup>4+</sup>/SnO<sub>2</sub> in TiO<sub>2</sub> could facilitate the phase transformation from anatase to rutile effectively at relatively low temperature [46,47]. Inspired by these

impressive advantages of SnO<sub>2</sub>, we conceive a new idea to prepare a highly effective  $\alpha$ -Fe<sub>2</sub>O<sub>3</sub>/SnO<sub>2</sub> catalyst for photo-Fenton system by innovatively encapsulating PB-derived Fe<sub>2</sub>O<sub>3</sub> nanocubes with SnO<sub>2</sub> shells. It is expected that SnO<sub>2</sub> shells can not only preserve the porous Fe<sub>2</sub>O<sub>3</sub> nanocubes from high-temperature treatment, but also promote the phase transformation of Fe<sub>2</sub>O<sub>3</sub> from metastable  $\beta$ -/ $\gamma$ -phases to stable  $\alpha$ -phase and stimulate the positive synergistic effect.

Following this design concept, we report herein the successful construction of core/shell  $\alpha$ -Fe<sub>2</sub>O<sub>3</sub>@SnO<sub>2</sub> nanocubes with tunable thickness of SnO<sub>2</sub> shells. The intact nanocubes and overwhelming  $\alpha$ -phase composition in  $\alpha$ -Fe<sub>2</sub>O<sub>3</sub>@SnO<sub>2</sub> nanocubes validate that SnO<sub>2</sub> shells indeed play a very crucial role in improving stability and accelerating phase transformation. By optimizing the annealing temperature and shells thickness,  $\alpha$ -Fe<sub>2</sub>O<sub>3</sub>@SnO<sub>2</sub> nanocubes could exhibit excellent catalytic performance in photo-Fenton system for the degradation of Rhodamine B (RhB). We believe that the as-prepared  $\alpha$ -Fe<sub>2</sub>O<sub>3</sub>@SnO<sub>2</sub> nanocubes can be a promising candidate for heterogeneous catalysts in photo-Fenton system for environmental remediation and the results may open up a new avenue for the design and preparation of various potential catalysts with great application prospects.

## 2. Experimental section

### 2.1. Synthesis of Fe<sub>2</sub>O<sub>3</sub>@SnO<sub>2</sub> nanocubes

PB nanocubes were firstly prepared according to previous literature [32,48]. In a typical recipe, 30.4 g of polyvinylpyrrolidone (PVP, K30) and 0.88 g of potassium hexacyanoferrate (II) were dissolved in 400 mL of HCl solution (0.1 M) under magnetic stirring. After 30 min, the clear solution was transferred into a glass bottle (500 mL), sealed and heated at 80 °C for 24 h to obtain the PB suspension. When the glass bottle was cooled down to room temperature, the required amount of stannous chloride dihydrate was slowly added into the PB suspension and the mixture was continuously stirred at room temperature for another 24 h. Then, the obtained blue products were collected by filtration, washed with distilled water and absolute ethanol for several times, and dried in a vacuum drier at 60 °C for 10 h. In the end, these blue products were calcined at 550 °C in air with a temperate ramp of 2 °C min<sup>-1</sup> for 6 h. The final samples were denoted as Fe<sub>2</sub>O<sub>3</sub>@SnO<sub>2</sub>(Sn- $x$ ), where  $x$  represented the mass of stannous chloride dihydrate. For example, the nomenclature of Fe<sub>2</sub>O<sub>3</sub>@SnO<sub>2</sub>(Sn-0.68) means that the mass of stannous chloride dihydrate is 0.68 g. For comparison, pure Fe<sub>2</sub>O<sub>3</sub> derived from PB [Fe<sub>2</sub>O<sub>3</sub>(PB)] was also prepared under the same conditions without the addition of stannous chloride dihydrate.

### 2.2. Characterization

The powder X-ray diffraction (XRD) patterns were measured on an X'PERT PRO MPD X-ray diffractometer with a Cu K $\alpha$  radiation source ( $\lambda$  = 1.5406 Å) (PANalytical B.V.). Scanning electron microscopy (SEM) images and energy dispersive spectra (EDS) were performed on a HELIOS NanoLab 600i (FEI). Transmission electron microscopy (TEM) images and high-resolution TEM (HRTEM) images were recorded by a Tecnai F20 operating at an accelerating voltage of 200 kV. Diffuse reflectance spectroscopy (DRS) was conducted on a UV/vis spectrophotometer (Shimadzu UV-2550) in the range of 200–800 nm. Photoluminescence (PL) spectra were recorded on LS55 Perkin Elmer (PE) Fluorescence Spectrometer with excitation wavelength of 400 nm. X-ray photoelectron spectra were obtained with PHI 5700 ESCA system equipped with an Al K $\alpha$  radiation as a source (1486.6 eV). Inductively coupled plasma atomic emission spectroscopy (ICP-

AES) was measured on Perkin Elmer (PE) Optima 8300. Nitrogen adsorption isotherms were obtained at 196 °C on a QUADRAZORB SI-KR/MP (Quantachrome, USA). Samples were normally prepared for measurement by degassing at 120 °C. The DMPO (5,5-dimethyl-1-pyrroline-N-oxide) trapped EPR spectra were carried out using a Bruker EPR A200 spectrometer at room temperature, which was operated at X-field with a centred field at 3350 G and a sweep width of 100 G.

### 2.3. Catalytic tests

The photo-Fenton performance of Fe<sub>2</sub>O<sub>3</sub>@SnO<sub>2</sub> nanocubes was investigated by the degradation of RhB in a dark box. Controlled experiments of different catalysts and their degradation kinetics, concentration of H<sub>2</sub>O<sub>2</sub>, catalyst dosage, initial pH and temperature on RhB degradation performance were determined by batch experiments. If necessary, the pH value was adjusted by either 0.1 M HNO<sub>3</sub> or NaOH aqueous solution and recorded with a Leici pH meter (model PHS-25). In a typical run, 15 mg of catalyst was dispersed into 25 mL RhB solution (25 mg L<sup>-1</sup>) with assistant of ultrasonic for 5 min and stirred in a constant-temperature water bath for 30 min to establish the adsorption-desorption equilibrium. The reaction was initiated by adding certain amounts of H<sub>2</sub>O<sub>2</sub> aqueous solution and simultaneously turning on the Xenon lamp (MICROSOLAR300, Perfectlight Co., Ltd. China) equipped with a 400 nm long-pass filter. At given time intervals, 1 mL of the reaction mixture was withdrawn and centrifuged (10,000 r/min) to remove the catalyst and the used catalysts were collected and dried at 60 °C for reusage. The changes of maximum absorption peak at 554 nm in the UV-vis absorption spectra (TU-1901, PERSEE Co., Ltd. China) reflected the degradation of RhB, which can be calculated by the following equation:

$$\text{Degradation efficiency (\%)} = [(C_0 - C_t)/C_0] \times 100\% \quad (1)$$

## 3. Results and discussion

As reported, the obtained PB is consisted of well-defined nanocubes with very smooth surfaces, and their average size is *ca.* 500 nm (Fig. 1a). The intensive and sharp diffraction peaks can be perfectly matched with the standard pattern of PB (JCPDS No. 01-0239), and no additional impurity peaks are detected (Fig. 1b), suggesting the formation of high-purity Fe<sub>4</sub>[Fe(CN)<sub>6</sub>]<sub>3</sub> during the process of hydrothermal treatment. TEM image and selected-area electron diffraction (SAED) further confirm the normative cubic structure and single-crystalline characteristic of these PB nanocubes (Fig. 1c and d). It is very interesting that the smooth surfaces of PB nanocubes become relatively rough after the introduction of stannous chloride (Fig. S1a), which implies that the hydrolysis product, Sn(OH)Cl, has been attached on their surfaces successfully. Although the characteristic peaks of Sn(OH)Cl cannot be detected (Fig. S1b), EDS spectra of PB@Sn(OH)Cl indeed confirm the presence of considerable Sn and Cl species (Fig. S1c).

The high-temperature heat treatment can convert PB and PB@Sn(OH)Cl nanocubes into the corresponding metal oxides, while the resultant Fe<sub>2</sub>O<sub>3</sub>(PB) and Fe<sub>2</sub>O<sub>3</sub>@SnO<sub>2</sub> nanocubes present quite different morphology and microstructure (Fig. 2). In the absence of SnO<sub>2</sub>, it can be found that Fe<sub>2</sub>O<sub>3</sub>(PB) fails to inherit the original cubic structure from PB, and most nanocubes collapse after the high-temperature calcination (Fig. 2a). In contrast, Fe<sub>2</sub>O<sub>3</sub>@SnO<sub>2</sub>(Sn-0.34), Fe<sub>2</sub>O<sub>3</sub>@SnO<sub>2</sub>(Sn-0.68), and Fe<sub>2</sub>O<sub>3</sub>@SnO<sub>2</sub>(Sn-1.02) promise very intact nanocubes with slightly concave surfaces due to the shrinkage of internal particles during heat treatment (Fig. 2b-d), which suggests that SnO<sub>2</sub> shells derived from Sn(OH)Cl can survive the heat-treatment process and prevent the collapse of Fe<sub>2</sub>O<sub>3</sub> nanocubes. From an occasionally

broken nanocube, the encapsulated microstructure with a SnO<sub>2</sub> shell and cross-linked Fe<sub>2</sub>O<sub>3</sub> nanoparticles can be clearly identified (Fig. S2), further confirming the considerable contribution from SnO<sub>2</sub> shells to the enhanced thermal stability. In addition, the sizes of these encapsulated composites display a gradual increase with more stannous chloride applied in the experiments. TEM images of Fe<sub>2</sub>O<sub>3</sub>(PB), Fe<sub>2</sub>O<sub>3</sub>@SnO<sub>2</sub>(Sn-0.34), Fe<sub>2</sub>O<sub>3</sub>@SnO<sub>2</sub>(Sn-0.68), and Fe<sub>2</sub>O<sub>3</sub>@SnO<sub>2</sub>(Sn-1.02) are also presented in order to acquire a comprehensive understanding of their microstructures (Fig. 2e-h). These images provide quite similar results to those of SEM images, where Fe<sub>2</sub>O<sub>3</sub>(PB) shows scattered nanoparticles from the collapsed nanocubes, and Fe<sub>2</sub>O<sub>3</sub>@SnO<sub>2</sub>(Sn-0.34), Fe<sub>2</sub>O<sub>3</sub>@SnO<sub>2</sub>(Sn-0.68), and Fe<sub>2</sub>O<sub>3</sub>@SnO<sub>2</sub>(Sn-1.02) are insusceptible to the high-temperature calcination. The abundant pores resulted from the decomposition of organic species can be clearly discerned inside these encapsulated Fe<sub>2</sub>O<sub>3</sub>@SnO<sub>2</sub> nanocubes, which may favor the diffusion of the reaction substrates and enhance the catalytic effectiveness. The magnified TEM insets of Fig. 2f-h indicate that the thickness of SnO<sub>2</sub> shells for Fe<sub>2</sub>O<sub>3</sub>@SnO<sub>2</sub>(Sn-0.34), Fe<sub>2</sub>O<sub>3</sub>@SnO<sub>2</sub>(Sn-0.68), and Fe<sub>2</sub>O<sub>3</sub>@SnO<sub>2</sub>(Sn-1.02) is 25 nm, 38 nm, and 55 nm, respectively. This means that with proper control of the relative ratios of stannous chloride and PB nanocubes, SnO<sub>2</sub> shells can be well fabricated on the nanocubes and the shell thickness can be modulated at the nanoscale. EDS and ICP-AES techniques are utilized to determine the chemical compositions of various composites. As shown in Fig. S3, EDS spectra demonstrate that the mass contents of Fe<sub>2</sub>O<sub>3</sub> and SnO<sub>2</sub> in Fe<sub>2</sub>O<sub>3</sub>@SnO<sub>2</sub>(Sn-0.34), Fe<sub>2</sub>O<sub>3</sub>@SnO<sub>2</sub>(Sn-0.68), and Fe<sub>2</sub>O<sub>3</sub>@SnO<sub>2</sub>(Sn-1.02) are 87.5% and 12.5%, 80.2% and 19.8%, and 68.9% and 31.1%, respectively. It is very interesting that ICP-AES gives similar chemical compositions (Table S1). The incremental content of SnO<sub>2</sub> is well consistent with the change of shell thickness. A closer inspection on the interface by high-resolution TEM reveals that the lattice fringes of internal nanoparticles (0.37 nm) and external shells (0.26 nm) can correspond to the (012) plane of α-Fe<sub>2</sub>O<sub>3</sub> and (101) plane of SnO<sub>2</sub> (Fig. 2i), respectively, indicating that Fe and Sn species in the precursor are preferentially converted into individual metal oxides rather than solid solution. The results of the elemental mapping also support that Fe is uniformly dispersed in internal core and Sn is primarily distributed in external shells (Fig. 2j-l). Although SnO<sub>2</sub> shells seem dense (Fig. S2), there are still many small mesopores resulted by the interspaces among these small SnO<sub>2</sub> nanoparticles (Fig. S4), and thus the reaction channel for α-Fe<sub>2</sub>O<sub>3</sub> and H<sub>2</sub>O<sub>2</sub> will not be blocked by these shells.

The crystalline structures of Fe<sub>2</sub>O<sub>3</sub>(PB) and Fe<sub>2</sub>O<sub>3</sub>@SnO<sub>2</sub> nanocubes are identified by XRD. As shown in Fig. 3, the diffraction pattern of Fe<sub>2</sub>O<sub>3</sub>(PB) can be associated with three different kinds of Fe<sub>2</sub>O<sub>3</sub>, *i.e.* α-Fe<sub>2</sub>O<sub>3</sub> (JCPDS No. 33-0664), β-Fe<sub>2</sub>O<sub>3</sub> (JCPDS No. 39-0238), and γ-Fe<sub>2</sub>O<sub>3</sub> (JCPDS No. 39-1346), which indicates that Fe<sub>2</sub>O<sub>3</sub> with mixed phase will be yielded under current conditions [32]. Interestingly, the characteristic peaks of α-Fe<sub>2</sub>O<sub>3</sub> will become overwhelming in Fe<sub>2</sub>O<sub>3</sub>@SnO<sub>2</sub> nanocubes, especially for Fe<sub>2</sub>O<sub>3</sub>@SnO<sub>2</sub>(Sn-1.02), the peaks of β-Fe<sub>2</sub>O<sub>3</sub> and γ-Fe<sub>2</sub>O<sub>3</sub> almost disappear. Although the specific mechanism is still unclear, it can be concluded that SnO<sub>2</sub> shells have positive effect on the phase transformation from β-/γ-Fe<sub>2</sub>O<sub>3</sub> to α-Fe<sub>2</sub>O<sub>3</sub>. A small peak at  $2\theta = 26.6^\circ$  assigned to (110) plane will not be detected until the dosage of stannous chloride reaches 0.68 g (marked by a red square), because SnO<sub>2</sub> generally has very small particle size (5–10 nm) and performs weak diffraction peaks [49,50]. It is well known that the calcination temperature always plays a very important role in determining the morphology and crystalline phase of metal oxides, and thus we attempt to prepare Fe<sub>2</sub>O<sub>3</sub>(PB) and Fe<sub>2</sub>O<sub>3</sub>@SnO<sub>2</sub>(Sn-0.68) at different temperature. When the temperature is reduced to 450 °C, Fe<sub>2</sub>O<sub>3</sub>(PB) will show typical porous nanocubes (Fig. S5a), while less α-Fe<sub>2</sub>O<sub>3</sub> is produced in the mix-phase product (Fig. S6a). If the tem-

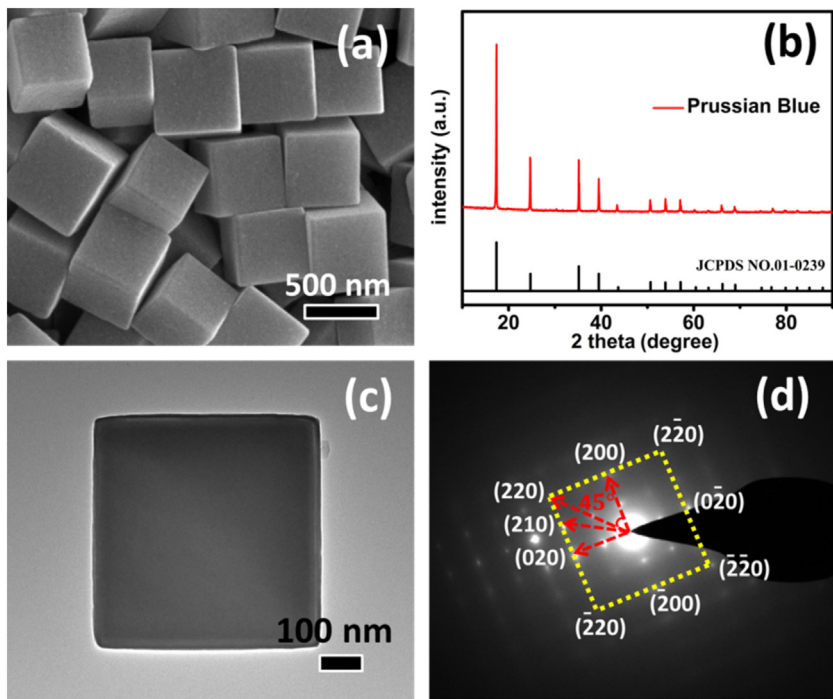


**Fig. 1.** SEM image (a), XRD pattern (b), TEM image (c), and Selected-area electron diffraction (SAED) (d) of PB nanocubes.

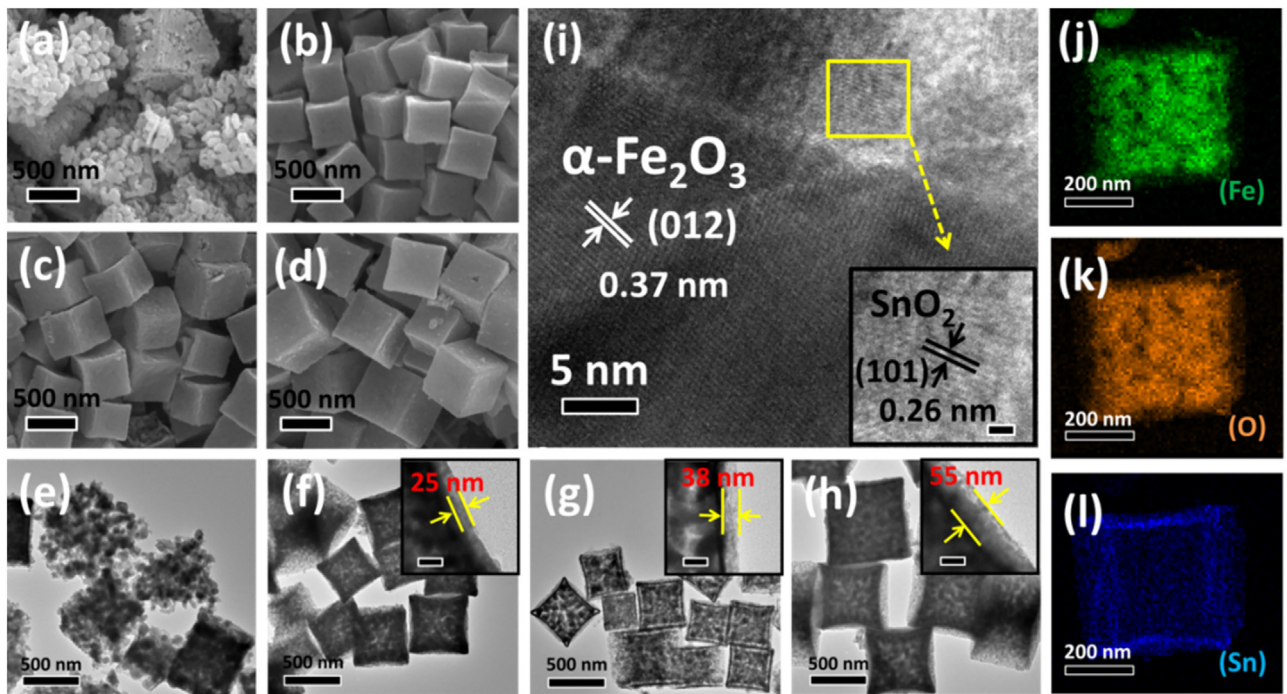


**Fig. 2.** SEM (a–d) and TEM (e–h) images of Fe<sub>2</sub>O<sub>3</sub>(PB) and Fe<sub>2</sub>O<sub>3</sub>@SnO<sub>2</sub> nanocubes; the insets of (f–h) are the thickness of SnO<sub>2</sub> shells in Fe<sub>2</sub>O<sub>3</sub>@SnO<sub>2</sub>(Sn-0.34), Fe<sub>2</sub>O<sub>3</sub>@SnO<sub>2</sub>(Sn-0.68), and Fe<sub>2</sub>O<sub>3</sub>@SnO<sub>2</sub>(Sn-1.02); HRTEM image (i) of Fe<sub>2</sub>O<sub>3</sub>@SnO<sub>2</sub>(Sn-0.68); elemental mapping images (j–k) of Fe, O and Sn in single Fe<sub>2</sub>O<sub>3</sub>@SnO<sub>2</sub>(Sn-0.68). The scale bars for the inset of (i) is 1 nm and (f–h) are 50 nm.

perature is increased to 650 °C, the cubic morphology will be totally lost and the scattering nanoparticles will be sintered into large particles (Fig. S5c). In despite of that, some peaks assigned to  $\beta$ -Fe<sub>2</sub>O<sub>3</sub> and  $\gamma$ -Fe<sub>2</sub>O<sub>3</sub> can still be easily distinguished (Fig. S6b). By comparison, no matter under 450 °C or 650 °C, Fe<sub>2</sub>O<sub>3</sub>@SnO<sub>2</sub>(Sn-0.68) can preserve its microstructure (Fig. S5b and d) and accomplish the transformation from  $\beta$ -/  $\gamma$ -Fe<sub>2</sub>O<sub>3</sub> to  $\alpha$ -Fe<sub>2</sub>O<sub>3</sub> simultaneously (Fig. S6). It is obvious that employing SnO<sub>2</sub> shells may be a bet-

ter choice to produce desirable structure and crystalline phase for PB-derived Fe<sub>2</sub>O<sub>3</sub>. According to the results of SEM, TEM, and XRD, the specific contribution of SnO<sub>2</sub> shells is schematically depicted in Fig. 4, where SnO<sub>2</sub> shells assume dual functions in both stabilizing microstructure and promoting phase transformation.

The optical absorption properties of home-made SnO<sub>2</sub>[SnO<sub>2</sub>(h)], Fe<sub>2</sub>O<sub>3</sub>(PB), and Fe<sub>2</sub>O<sub>3</sub>@SnO<sub>2</sub> nanocubes are investigated by UV-vis DRS spectra in Fig. S7. The absorption onset

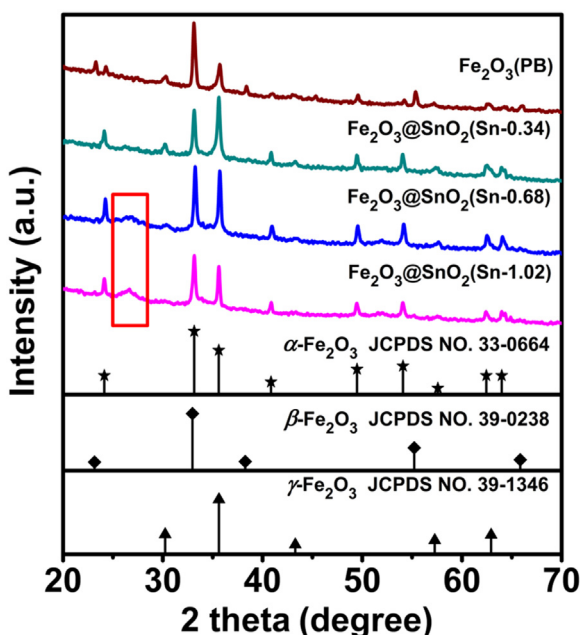


**Fig. 3.** The XRD patterns of  $\text{Fe}_2\text{O}_3(\text{PB})$  and  $\text{Fe}_2\text{O}_3@\text{SnO}_2$  nanocubes.

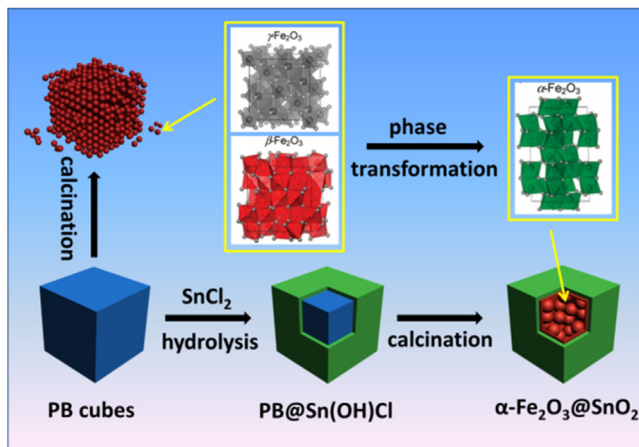


**Fig. 4.** Schematic illustration of the contribution of  $\text{SnO}_2$  shells to the microstructure and phase composition of internal  $\text{Fe}_2\text{O}_3$  nanocubes.

of  $\text{SnO}_2$  is found at about 350 nm, corresponding to its band gap energy of 3.6 eV [39,51]. In contrast,  $\text{Fe}_2\text{O}_3(\text{PB})$  exhibits a very broad band in the whole studied interval (200–800 nm), which can be attributed to the joint action of the  $d-d$  transitions, the ligand to metal charge-transfer transitions, and the pair excitations of two neighboring  $\text{Fe}^{3+}$  cations [52]. It is very interesting that  $\text{Fe}_2\text{O}_3@\text{SnO}_2$  nanocubes with different thickness of  $\text{SnO}_2$  shells almost inherit all absorption characteristics from inside  $\text{Fe}_2\text{O}_3$  and display quite similar absorption bands, indicating that  $\text{SnO}_2$  shells in these composites will not restrain the light absorption of  $\text{Fe}_2\text{O}_3$ , especially in the visible region.

The chemical composition and elemental chemical status of  $\text{Fe}_2\text{O}_3@\text{SnO}_2(\text{Sn}-0.68)$  as a representative sample are further characterized by XPS. As shown in Fig. 5a, the survey of XPS spectrum reveals that  $\text{Fe}_2\text{O}_3@\text{SnO}_2(\text{Sn}-0.68)$  is only composed of elements such as Fe, Sn, and O [a high concentration of C is found due to the binding energy for C 1s (284.6 eV) as the internal reference (Fig. 5b)] [53], and no signals assigned to N and Cl can be detected, again verifying the complete transformation from  $\text{PB}@\text{Sn(OH)}\text{Cl}$  to  $\text{Fe}_2\text{O}_3@\text{SnO}_2$  without C and N doping. Fe 2p spectrum gives three

**Table 1**

The textural parameters of  $\text{Fe}_2\text{O}_3(\text{PB})$ ,  $\text{Fe}_2\text{O}_3@\text{SnO}_2$  nanocubes and commercial  $\text{Fe}_2\text{O}_3$  determined by  $\text{N}_2$  adsorption-desorption isotherms.

Sample	Surface area ( $\text{m}^2/\text{g}$ )	Pore volume ( $\text{cm}^3/\text{g}$ )
Commercial $\text{Fe}_2\text{O}_3$	9.06	0.159
$\text{Fe}_2\text{O}_3(\text{PB})$	22.69	0.156
$\text{Fe}_2\text{O}_3@\text{SnO}_2(\text{Sn}-0.34)$	28.18	0.250
$\text{Fe}_2\text{O}_3@\text{SnO}_2(\text{Sn}-0.68)$	37.30	0.296
$\text{Fe}_2\text{O}_3@\text{SnO}_2(\text{Sn}-1.02)$	24.34	0.260

typical peaks (Fig. 5c), where the peaks at 710.5 eV and 723.9 eV can be indexed to  $\text{Fe } 2p_{3/2}$  and  $\text{Fe } 2p_{1/2}$  of  $\text{Fe}^{3+}$  in  $\alpha\text{-Fe}_2\text{O}_3$  [38], and the stronger peak with binding energy of 715.5 eV is ascribed to  $\text{Sn } 3p_{3/2}$  (Fig. 5c). It is worth noting that although  $\text{Fe}_2\text{O}_3$  has larger mass fraction than  $\text{SnO}_2$  in  $\text{Fe}_2\text{O}_3@\text{SnO}_2(\text{Sn}-0.68)$  (Fig. S3), the shielding effect caused by  $\text{SnO}_2$  shells leads to its relatively weak signals. The binding energies of  $\text{Sn } 3d_{5/2}$  and  $\text{Sn } 3d_{3/2}$  located at 486.1 eV and 494.5 eV (Fig. 5d), respectively, confirm that Sn species in  $\text{Fe}_2\text{O}_3@\text{SnO}_2(\text{Sn}-0.68)$  are tetravalent [53]. These results are in good agreement with those of XRD.

Fig. 6 shows  $\text{N}_2$  adsorption-desorption isotherms of  $\text{Fe}_2\text{O}_3(\text{PB})$  and  $\text{Fe}_2\text{O}_3@\text{SnO}_2$  nanocubes, and their specific BET surface area and pore volume are listed in Table 1. All samples give isotherms between II-type and IV-type according to the IUPAC classification, and their long and narrow hysteresis loops at high relative pressure ( $P/P_0 > 0.8$ ) means that their pore size distributions are not uniform [54–56]. Compared with the commercial  $\text{Fe}_2\text{O}_3$ ,  $\text{Fe}_2\text{O}_3(\text{PB})$  perform improved BET surface area ( $22.69 \text{ m}^2/\text{g}$ ) and similar pore volume ( $0.156 \text{ cm}^3/\text{g}$ ), suggesting that  $\text{Fe}_2\text{O}_3(\text{PB})$  may have smaller particle size than commercial  $\text{Fe}_2\text{O}_3$ . In the presence of  $\text{SnO}_2$  shells, BET surface area and pore volume of  $\text{Fe}_2\text{O}_3@\text{SnO}_2$  nanocubes can be further increased. Although  $\text{SnO}_2$  shells are relatively dense (Fig. 2), it is worth noting that the pore volumes of  $\text{Fe}_2\text{O}_3@\text{SnO}_2$  nanocubes are obviously superior to that of  $\text{Fe}_2\text{O}_3(\text{PB})$ , which forcefully validates the successful preservation of porous microstructure in the composites under the assistance of  $\text{SnO}_2$  shells. However, for  $\text{Fe}_2\text{O}_3@\text{SnO}_2(\text{Sn}-1.02)$ , the thickened  $\text{SnO}_2$  shells suppress the absorbed contribution of internal  $\text{Fe}_2\text{O}_3$  nanocubes, and thus the BET surface and pore volume present slight decrease.

Fig. 7a shows RhB degradation via catalytic photo-Fenton process with different catalysts. Although some existing reports illustrated that  $\text{Fe}_3\text{O}_4$  and  $\text{Fe}_2\text{O}_3$  were good heterogeneous catalysts for the degradation of organic pollutants in Fenton system [57–60], commercial  $\text{Fe}_3\text{O}_4$  [ $\text{Fe}_3\text{O}_4(\text{c})$ ] and  $\alpha\text{-Fe}_2\text{O}_3$  [ $\alpha\text{-Fe}_2\text{O}_3(\text{c})$ ] (their XRD patterns are showed in Fig. S8) herein does not present impressive catalytic efficiency under current conditions and only less than 30% of RhB is removed in 60 min. When  $\text{Fe}_2\text{O}_3(\text{PB})$  is employed as the heterogeneous catalyst, RhB degradation can be increased to 88.6% in 60 min. It is very interesting that with the appearance of  $\text{SnO}_2$  shells,  $\text{Fe}_2\text{O}_3@\text{SnO}_2(\text{Sn}-0.34)$ ,  $\text{Fe}_2\text{O}_3@\text{SnO}_2(\text{Sn}-0.68)$  and  $\text{Fe}_2\text{O}_3@\text{SnO}_2(\text{Sn}-1.02)$  contribute to more powerful RhB degradation, so that the degradation efficiencies can reach up to 97.1%, 99.7%, and 98.3% in 60 min, respectively. Even in 30 min, their degradation efficiencies are still 80.5%, 97.4%, and 86.8%, indicating the excellent photo-Fenton activity of  $\text{Fe}_2\text{O}_3@\text{SnO}_2$  nanocubes. By considering the features of  $\text{Fe}_2\text{O}_3@\text{SnO}_2$  nanocubes, there are several important factors, e.g.  $\text{SnO}_2$  shells, crystalline phase, microstructure, and the synergistic effect between  $\text{Fe}_2\text{O}_3$  and  $\text{SnO}_2$ , which may be responsible for the significant enhancement in catalytic ability. The direct contribution from  $\text{SnO}_2$  shells is easily excluded because individual  $\text{SnO}_2(\text{h})$  fabricated by the same method only presents RhB degradation at 16.9% in 60 min, which is very close to the degradation efficiency in blank  $\text{H}_2\text{O}_2/\text{vis}$  system (12.6%, Fig. 7d). The negligible increase of RhB removal in  $\text{SnO}_2(\text{h})/\text{H}_2\text{O}_2/\text{vis}$  system may be attributed to the physical absorption on the surface of  $\text{SnO}_2(\text{h})$ . Therefore,  $\text{Fe}_2\text{O}_3$  in  $\text{Fe}_2\text{O}_3@\text{SnO}_2$

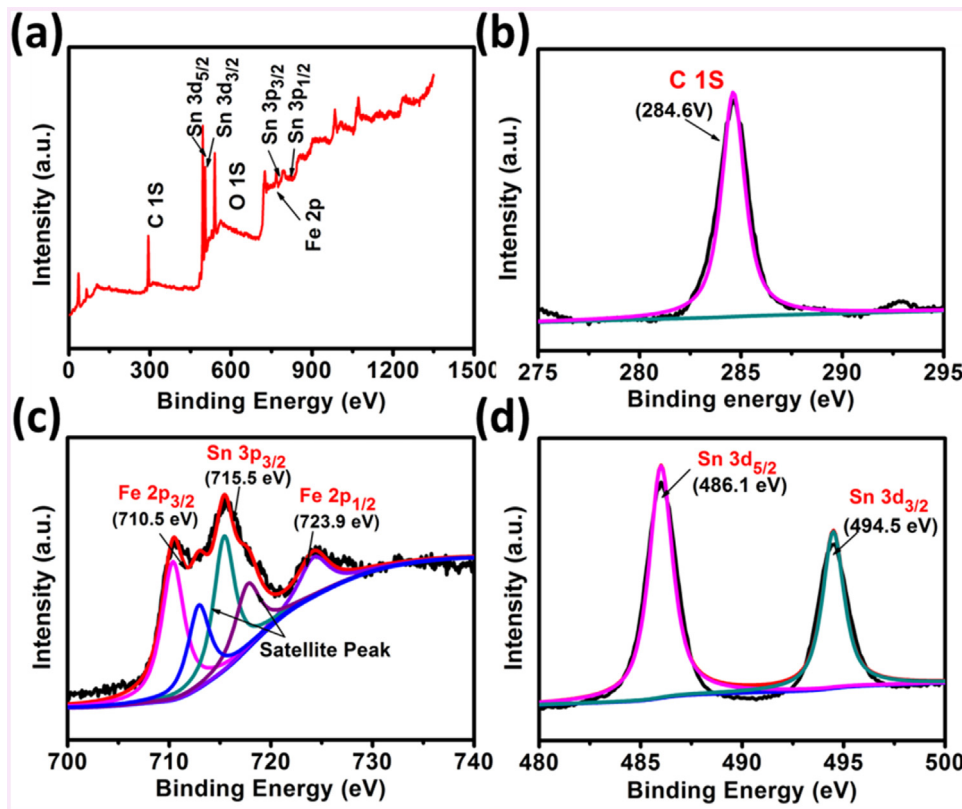


**Fig. 5.** XPS spectra of  $\text{Fe}_2\text{O}_3@\text{SnO}_2$  (Sn-0.68). Survey spectrum (a), C 1s (b), Fe 2p (c), and Sn 3d (d).

nanocubes can be taken as the primary active sites for the activation of  $\text{H}_2\text{O}_2$ . However, PB-derived pure  $\text{Fe}_2\text{O}_3$  catalysts from different calcination temperature perform quite different RhB degradation. For example,  $\text{Fe}_2\text{O}_3$ -450 comprised of  $\beta$ - $\text{Fe}_2\text{O}_3$  and  $\gamma$ - $\text{Fe}_2\text{O}_3$  only accounts for 13.9% of RhB degradation in 60 min, and  $\text{Fe}_2\text{O}_3$ -650 with preponderant  $\alpha$ -phase promises the degradation of RhB at 94.1% in 60 min (Fig. S6 and S9). These results forcefully prove that  $\alpha$ -phase of  $\text{Fe}_2\text{O}_3$  is more favorable for the activation of  $\text{H}_2\text{O}_2$  than  $\beta$ - $\text{Fe}_2\text{O}_3$  and  $\gamma$ - $\text{Fe}_2\text{O}_3$ . Although increasing calcination temperature is an effective route for phase transformation from  $\beta$ - $\text{Fe}_2\text{O}_3/\gamma$ - $\text{Fe}_2\text{O}_3$  to  $\alpha$ - $\text{Fe}_2\text{O}_3$ , it also induces the shrinkage/collapse of the microstructure, resulting in a negative impact on the catalytic activity of  $\text{Fe}_2\text{O}_3$ . In view of this fact,  $\alpha$ - $\text{Fe}_2\text{O}_3$ (c) with high-purity  $\alpha$ -phase still performs less RhB degradation than  $\text{Fe}_2\text{O}_3$ (PB) with mixed crystalline phase, because the advantage of  $\alpha$ - $\text{Fe}_2\text{O}_3$ (c) in crystalline phase cannot cover its shortage of dense microstructure (Table 1). The trade-off relationship between the phase optimization and the microstructure always makes it difficult to fully develop the potential of  $\text{Fe}_2\text{O}_3$ . As revealed by XRD, SEM, and TEM,  $\text{SnO}_2$  shells in these composites assume dual functions in both stabilizing microstructure and promoting phase transformation, and the preferable  $\alpha$ -phase can be obtained with less damage on the microstructure. Therefore,  $\text{Fe}_2\text{O}_3$  in  $\text{Fe}_2\text{O}_3@\text{SnO}_2$  nanocubes will possess more advantages in heterogeneous photo-Fenton reaction than pure  $\text{Fe}_2\text{O}_3$  derived from PB. That is to say,  $\text{SnO}_2$  shells provide an indirect contribution to the simultaneous optimization on the crystalline phase and the microstructure of  $\text{Fe}_2\text{O}_3$ , which are responsible for the enhanced catalytic activity of  $\text{Fe}_2\text{O}_3@\text{SnO}_2$  nanocubes. This superiority is even applicable to  $\text{Fe}_2\text{O}_3@\text{SnO}_2$  nanocubes obtained at different calcination temperature (Fig. S9).

In addition, it is widely accepted that the synergistic effect between  $\alpha$ - $\text{Fe}_2\text{O}_3$  and  $\text{SnO}_2$  will also contribute to the catalytic activity of  $\text{Fe}_2\text{O}_3/\text{SnO}_2$  composites, because the heterojunction can

reduce the recombination of photo-generated electrons and holes [42,61,62]. As shown in Fig. S10, photoluminescence (PL) spectra are utilized to investigate the synergistic effect between  $\alpha$ - $\text{Fe}_2\text{O}_3$  and  $\text{SnO}_2$ . The magnificent band for bare  $\text{Fe}_2\text{O}_3$ (PB) reveals that  $\text{Fe}_2\text{O}_3$  can be excited by visible light as a photo-catalyst with a fast recombination rate of photo-generated electron-hole pairs. When  $\text{SnO}_2$  shells are introduced to the composites,  $\text{Fe}_2\text{O}_3@\text{SnO}_2$  nanocubes show a relatively weak PL intensity, suggesting that the recombination of photo-generated electron-hole pairs may be moderately suppressed in the composites. The conduction band of  $\text{SnO}_2$  can act as a sink for photo-generated electrons, and the photo-generated holes will move to the opposite direction and accumulate in the valence band of  $\alpha$ - $\text{Fe}_2\text{O}_3$ . The separated photo-generated electrons and holes have also been confirmed to work for the activation of  $\text{H}_2\text{O}_2$  to release  $\text{HO}^\bullet$  [63]. However, it has to mention that the PL intensities of  $\text{Fe}_2\text{O}_3@\text{SnO}_2$  nanocubes are not sharply decreased and even slightly increase with more  $\text{SnO}_2$  loading. These phenomena may be explained by two aspects: (1) the core-shell microstructure of  $\text{Fe}_2\text{O}_3@\text{SnO}_2$  nanocubes cannot provide the homogeneous dispersion of  $\text{SnO}_2$  and  $\text{Fe}_2\text{O}_3$  nanoparticles, and thus their synergistic effect will be limited due to the insufficient heterogeneous interfaces; (2)  $\text{SnO}_2$  itself cannot be excited by visible light (excitation of 400 nm), and excessive loading of  $\text{SnO}_2$  may not promote the separation of the photo-generated electrons and holes continuously, but hinder their transmissions. Similar phenomenon can be observed in the composites of  $\text{Fe}_2\text{O}_3/\text{NiTiO}_3$  [64]. In order to evaluate the contribution from the synergistic effect in  $\text{Fe}_2\text{O}_3@\text{SnO}_2$  nanocubes, we also prepare a control sample of  $\text{Fe}_2\text{O}_3/\text{SnO}_2$  composite with similar chemical composition to  $\text{Fe}_2\text{O}_3@\text{SnO}_2$ (Sn-0.68) through co-precipitation method, which can produce more homogeneous distribution of  $\text{SnO}_2$  and  $\text{Fe}_2\text{O}_3$  nanoparticles as compared with  $\text{Fe}_2\text{O}_3@\text{SnO}_2$  nanocubes. PL spectra confirms that  $\text{Fe}_2\text{O}_3/\text{SnO}_2$  composite indeed displays a lower

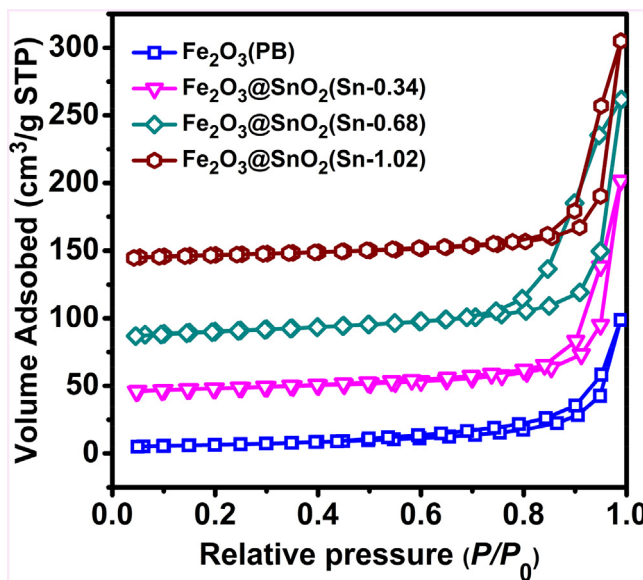


**Fig. 6.**  $\text{N}_2$  adsorption-desorption isotherms of  $\text{Fe}_2\text{O}_3(\text{PB})$  and  $\text{Fe}_2\text{O}_3@\text{SnO}_2$  nanocubes. The isotherms of  $\text{Fe}_2\text{O}_3@\text{SnO}_2(\text{Sn}-0.34)$ ,  $\text{Fe}_2\text{O}_3@\text{SnO}_2(\text{Sn}-0.68)$  and  $\text{Fe}_2\text{O}_3@\text{SnO}_2(\text{Sn}-1.02)$  remove upwards 40, 80, and  $140 \text{ cm}^3/\text{g}$  at the beginning for clarity, respectively.

recombination rate of photo-generated electrons and holes than  $\text{Fe}_2\text{O}_3@\text{SnO}_2(\text{Sn}-0.68)$  (Fig. S11a), while the degradation of RhB over  $\text{Fe}_2\text{O}_3/\text{SnO}_2$  composite is far behind that over  $\text{Fe}_2\text{O}_3@\text{SnO}_2(\text{Sn}-0.68)$ , even much less than that over pure  $\text{Fe}_2\text{O}_3$  derived PB (Fig. S11b). Based on these results, it can be concluded that the synergistic effect between  $\alpha\text{-Fe}_2\text{O}_3$  and  $\text{SnO}_2$  may be helpful to improve the activation of  $\text{H}_2\text{O}_2$ , but the enhanced catalytic activity in  $\text{Fe}_2\text{O}_3@\text{SnO}_2$  nanocubes should be more dependent on the simultaneous optimizations of the crystalline phase and the microstructure induced by  $\text{SnO}_2$  shells.

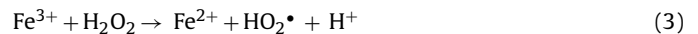
In general, the degradation of organic dye obeys the pseudo-first order kinetics [65], and thus the kinetics constant over various catalysts can be calculated by the following equation:

$$\ln(C_0/C_t) = kt \quad (2)$$

where  $C_0$  is the initial dye concentration reached adsorption-desorption equilibrium in dark,  $C_t$  is the dye concentration at given time  $t$  during the Fenton process, and  $k$  is the reaction rate constant. The results show that the kinetic rate constants of  $\text{Fe}_2\text{O}_3@\text{SnO}_2(\text{Sn}-0.34)$  ( $0.061 \text{ min}^{-1}$ ),  $\text{Fe}_2\text{O}_3@\text{SnO}_2(\text{Sn}-0.68)$  ( $0.090 \text{ min}^{-1}$ ), and  $\text{Fe}_2\text{O}_3@\text{SnO}_2(\text{Sn}-1.02)$  ( $0.081 \text{ min}^{-1}$ ) are 12–30 times higher than those of  $\text{Fe}_3\text{O}_4(\text{c})$  ( $0.003 \text{ min}^{-1}$ ),  $\text{Fe}_2\text{O}_3(\text{c})$  ( $0.005 \text{ min}^{-1}$ ),  $\text{SnO}_2(\text{c})$  ( $0.003 \text{ min}^{-1}$ ), and 1.7–2.5 times higher than that of  $\text{Fe}_2\text{O}_3(\text{PB})$  ( $0.036 \text{ min}^{-1}$ ) (Fig. 7b), further validating the positive effect of  $\text{SnO}_2$  shells on the catalytic efficiency. Of note is that the amount of  $\text{SnO}_2$ , namely the thickness of  $\text{SnO}_2$  shells, can affect the catalytic activity of  $\text{Fe}_2\text{O}_3@\text{SnO}_2$  nanocubes greatly, where  $\text{Fe}_2\text{O}_3@\text{SnO}_2(\text{Sn}-0.68)$  with moderate  $\text{SnO}_2$  shells indeed displays the best performance among the three samples. This phenomenon can be attributed to the two-sided effects of  $\text{SnO}_2$  shells in these composites. When the amount of  $\text{SnO}_2$  is 12.5%,  $\text{Fe}_2\text{O}_3@\text{SnO}_2(\text{Sn}-0.34)$  still contains considerable  $\gamma\text{-Fe}_2\text{O}_3$  (Fig. 3) that is incapable of activating  $\text{H}_2\text{O}_2$  (Fig. S9), and meanwhile,  $\text{Fe}_2\text{O}_3@\text{SnO}_2(\text{Sn}-0.34)$  also shows smaller surface area and pore volume than  $\text{Fe}_2\text{O}_3@\text{SnO}_2(\text{Sn}-0.68)$  (Table 1). These results indicate that current  $\text{SnO}_2$  amount cannot afford full phase transformation and microstructure stability. In contrast,  $\text{Fe}_2\text{O}_3@\text{SnO}_2(\text{Sn}-0.68)$  displays almost single  $\alpha$ -phase and abundant porous microstructure, which is naturally favorable for the catalytic process, and thus its catalytic activity can be significantly

enhanced. Although the phase transformation will be completely achieved with further increasing the amount of  $\text{SnO}_2$ , excessive loading of  $\text{SnO}_2$  not only produces very dense shells (Fig. 2h) and suppresses the diffusion of reaction substance, but also decreases the real content of active  $\alpha\text{-Fe}_2\text{O}_3$  applied in the catalytic system [68.9 wt% in  $\text{Fe}_2\text{O}_3@\text{SnO}_2(\text{Sn}-1.02)$ ] because the dosage of catalyst is fixed at 15.0 mg for every batch experiment. Both of these two facts will weaken the catalytic activity of  $\text{Fe}_2\text{O}_3@\text{SnO}_2(\text{Sn}-1.02)$ . Fig. 7c shows UV-vis spectra of the characteristic peak of RhB over the catalyst of  $\text{Fe}_2\text{O}_3@\text{SnO}_2(\text{Sn}-0.68)$ , and it is found that the intensity of the characteristic peak decreases gradually and presents a slight blue shift with increasing irradiation time, indicating that RhB is decomposed through direct cleavage of the conjugated chromophore structure [66,67]. The UV-vis spectra of RhB degradation over other kinds of catalyst are presented in Fig. S12. The degradation of RhB is also carried out under different conditions, as shown in Fig. 7d, negligible RhB will be removed in the absence of visible light and  $\text{H}_2\text{O}_2$ , which means that the contributions from direct  $\text{H}_2\text{O}_2$  oxidation and physical absorption are rather limited, and thus the radical-based oxidation process will be deduced as the primary pathway for RhB degradation. However, sole visible light irradiation still fails to active  $\text{H}_2\text{O}_2$  and release sufficient radicals, demonstrating that RhB degradation is essentially accomplished by a heterogeneous catalytic photo-Fenton process.

It has been verified that  $\text{Fe}_2\text{O}_3$  was referred to a classic Fenton-like reagent to induce the dissociation of hydrogen peroxide and generate highly reactive radicals that could attack and destroy the organic pollutants [68–71]. Based on these guidance works, the basic reaction mechanism could be summarized through the following chain reactions [68]:



It should be pointed out that the intermediate  $\text{HO}_2^\bullet$  species participated in the circular reactions of  $\text{Fe}^{2+}/\text{Fe}^{3+}$  (Eqs. (5) and (6)) are always constrained by a shorter lifetime, and therefore, hydroxyl radicals ( $\text{HO}^\bullet$ ) will be in charge of the catalytic oxidation of organic dyes (Eq. (7)). In order to ascertain the dominant reactive species in photo-Fenton system catalyzed by  $\text{Fe}_2\text{O}_3@\text{SnO}_2(\text{Sn}-0.68)$ , free radical quenching study and trapping examination are performed by employing methanol and DMPO as scavenger and spin-trapping agent during the hydrogen peroxide activation. As observed in Fig. 8a, the degradation efficiency of RhB present an obvious decrease from 99.7% to 66.3% as the concentration ratio of methanol to hydrogen peroxide is manipulated from 0:1 to 20:1. When the methanol concentration is 40 times of the hydrogen peroxide, the removal efficiency of RhB is almost completely suppressed, further validating the radical-based oxidation process. EPR spectra reveal that there are four well-defined peaks with 1:2:2:1 quarter pattern in  $\text{Fe}_2\text{O}_3@\text{SnO}_2(\text{Sn}-0.68)/\text{H}_2\text{O}_2$  system (Fig. 8b), which can be attributed to the characteristic signal of the DMPO/ $\text{HO}^\bullet$  adduct [72–74], while the related peaks cannot be detected in the absence of  $\text{Fe}_2\text{O}_3@\text{SnO}_2(\text{Sn}-0.68)$ . That is to say,  $\text{Fe}_2\text{O}_3@\text{SnO}_2(\text{Sn}-0.68)$  plays a crucial role in activating hydrogen peroxide to generate large amounts of  $\text{HO}^\bullet$  under current conditions. In view of above results, it can be concluded that  $\text{SnO}_2$  shells do not change the catalytic mechanism of  $\alpha\text{-Fe}_2\text{O}_3$  and  $\text{HO}^\bullet$  still works as the main reactive species for the degradation of RhB. The upgraded performance of  $\text{Fe}_2\text{O}_3@\text{SnO}_2(\text{Sn}-0.68)$  simply benefits from the stable microstructure and preferable crystalline phase. Furthermore, it is worth mentioning that  $\text{SnO}_2$  has negligible absorption in visible region

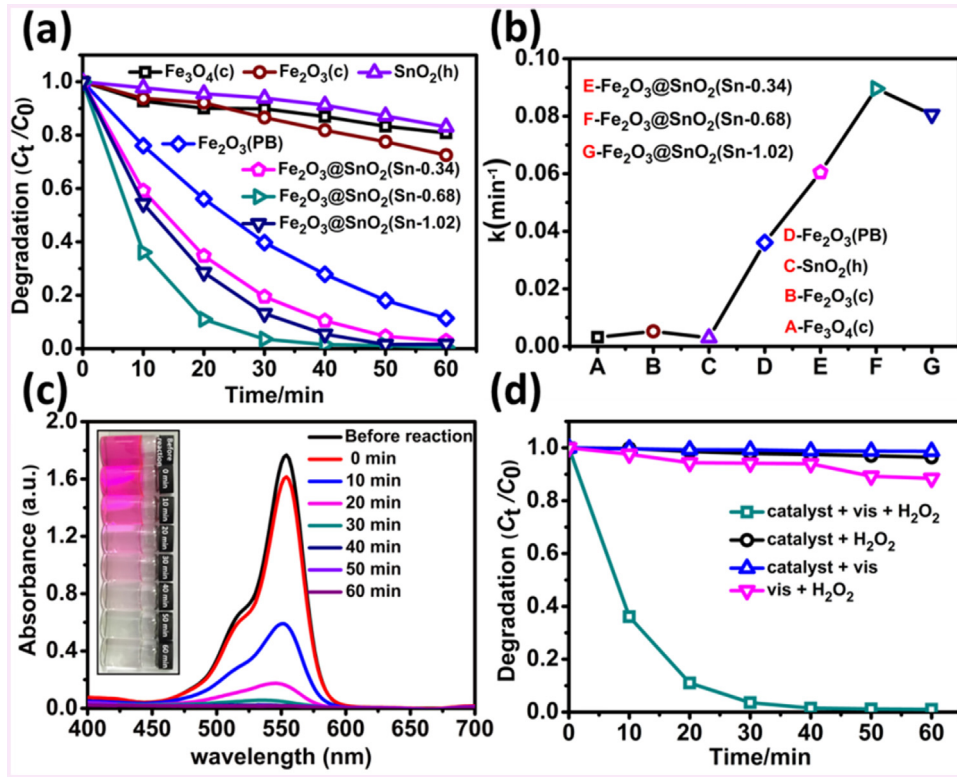


**Fig. 7.** The photo-Fenton activities (a) and rate constants (b) of Fe<sub>2</sub>O<sub>3</sub>(PB) and Fe<sub>2</sub>O<sub>3</sub>@SnO<sub>2</sub> nanocubes compared with Fe<sub>3</sub>O<sub>4</sub>(c), Fe<sub>2</sub>O<sub>3</sub>(c) and SnO<sub>2</sub>(h). The UV-vis spectrum of RhB degradation over Fe<sub>2</sub>O<sub>3</sub>@SnO<sub>2</sub>(Sn-0.68) (c), and the photo-Fenton properties of Fe<sub>2</sub>O<sub>3</sub>@SnO<sub>2</sub>(Sn-0.68) under different reaction conditions (d). Reaction conditions: [RhB] = 25 mg L<sup>-1</sup>, [H<sub>2</sub>O<sub>2</sub>] = 0.4 M, catalyst = 0.6 g L<sup>-1</sup>, T = 35 °C, pH = 7.33 and MICROSOLAR300 Xenon lamp: 19.6 mW cm<sup>-2</sup>.

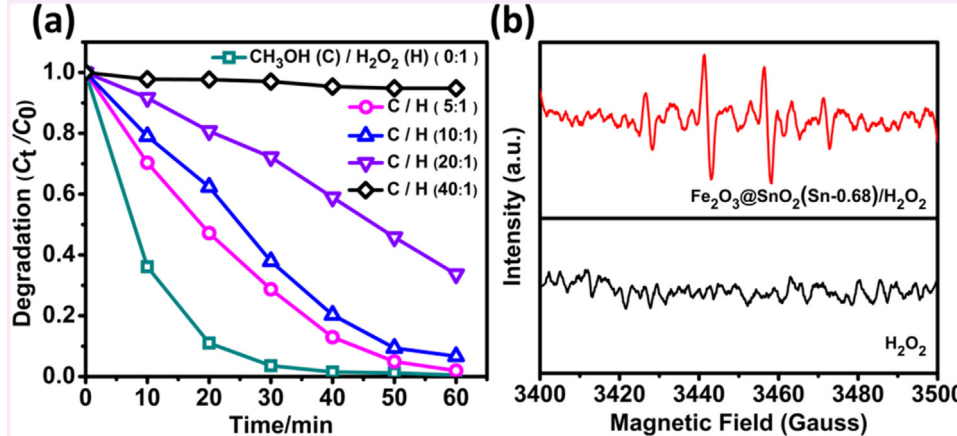


**Fig. 8.** The influence of radical scavenger of methanol to RhB degradation over Fe<sub>2</sub>O<sub>3</sub>@SnO<sub>2</sub>(Sn-0.68) (a); DMPO trapped EPR spectra of Fe<sub>2</sub>O<sub>3</sub>@SnO<sub>2</sub>(Sn-0.68)/H<sub>2</sub>O<sub>2</sub> system and H<sub>2</sub>O<sub>2</sub> system (b).

due to its wide band gap (~3.6 eV), thereby the visible light will unimpededly diffuse through SnO<sub>2</sub> shells and motivate the reactions on the surface of  $\alpha$ -Fe<sub>2</sub>O<sub>3</sub> (Fig. S7) [75,76].

In addition, the effects of H<sub>2</sub>O<sub>2</sub> concentration, catalyst dosage, pH value, and reaction temperature on RhB degradation of photo-assisted Fe<sub>2</sub>O<sub>3</sub>@SnO<sub>2</sub>(Sn-0.68)/H<sub>2</sub>O<sub>2</sub> are further studied. As shown in Fig. 9a, when the concentration of H<sub>2</sub>O<sub>2</sub> increases from 0.1 to 0.6 M, the degradation efficiency of RhB will be gradually enhanced from 80.5% to 93.7% in 30 min. It is reliable that increasing H<sub>2</sub>O<sub>2</sub> concentration will make more H<sub>2</sub>O<sub>2</sub> molecules attach to the active sites of  $\alpha$ -Fe<sub>2</sub>O<sub>3</sub>, which accelerates the generation of radical species. However, once H<sub>2</sub>O<sub>2</sub> concentration exceeds 0.6 M, more H<sub>2</sub>O<sub>2</sub> will not promote the degradation efficiency of RhB obviously any more.

This phenomenon can be explained from two aspects. On one hand, the active sites on the surface of catalyst are limited, and thus excessive H<sub>2</sub>O<sub>2</sub> cannot be activated to release more radical species. On the other hand, additional H<sub>2</sub>O<sub>2</sub> will undesirably consume partial HO<sup>•</sup> through the following reactions (Eqs. (8) and (9)) and consequently inhibit the catalytic oxidation process [68,77].



The catalyst dosage presents a similar effect on the degradation efficiency of RhB (Fig. 9b). For example, RhB degradation increases from 85.0% with 0.2 g/L of catalyst to 97.0% with 0.4 g/L of catalyst within 30 min, and maintains the comparable effectiveness

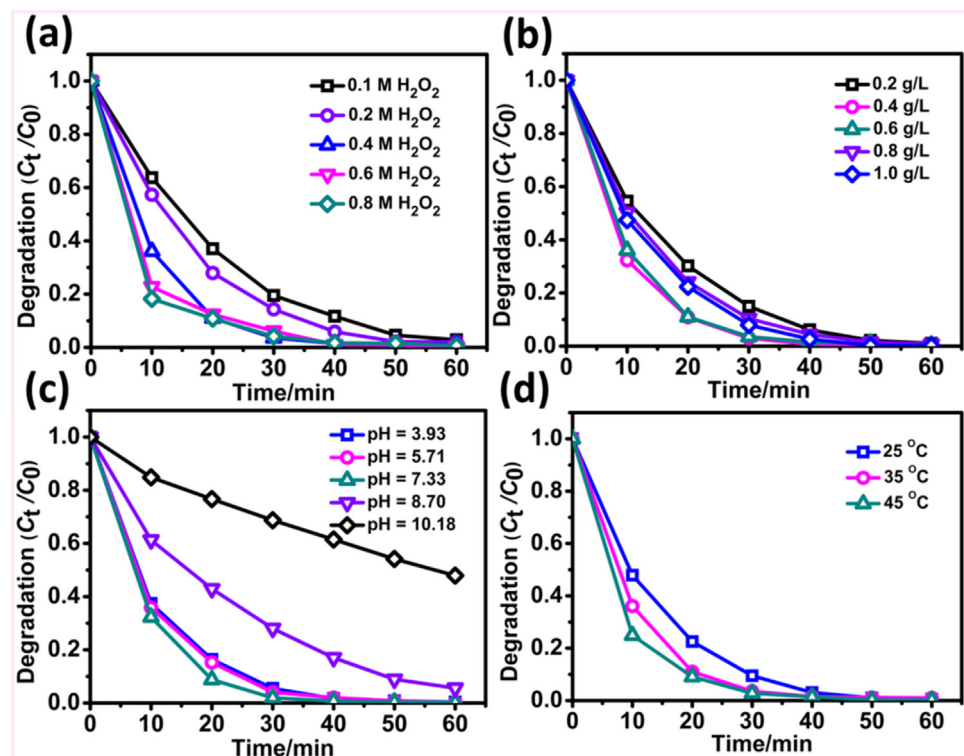


**Fig. 9.** The effect of  $\text{H}_2\text{O}_2$  concentration (a), catalyst dosage (b), initial pH (c), and reaction temperature (d) on RhB degradation in photo-Fenton system catalyzed by  $\text{Fe}_2\text{O}_3@\text{SnO}_2(\text{Sn}-0.68)$ . Reaction conditions:  $[\text{RhB}] = 25 \text{ mg L}^{-1}$ ,  $[\text{H}_2\text{O}_2] = 0.4 \text{ M}$ , catalyst  $= 0.6 \text{ g L}^{-1}$ ,  $\text{pH} = 7.33$  and MICROSOLAR300 Xenon lamp:  $19.6 \text{ mW cm}^{-2}$ .

(96.4%) with  $0.6 \text{ g/L}$  of catalyst, and then starts to decrease with more dosage of catalyst. Apparently, the increasing dosage of catalyst provides more active sites on the surface of  $\alpha\text{-Fe}_2\text{O}_3$  for  $\text{H}_2\text{O}_2$  to occupy, and thus more reactive species can be generated [78]. However, these active sites not only induce the formation of radical species, but also lead to an inverse consumption of radical species. According to previous literature, this phenomenon can be related to the diffusion limitation in heterogeneous reactions [79]. Specifically, when the catalyst dosage exceeds the critical value, the resultant radical species will preferentially interact with those active sites, and thus the ineffective oxidant consumption on the surface of  $\alpha\text{-Fe}_2\text{O}_3$  will be accelerated and become dominant before RhB arriving, leading to the decreased degradation efficiency [80,81]. Based on these systematical investigations, it is worth mentioning that either  $\text{H}_2\text{O}_2$  concentration or  $\text{Fe}_2\text{O}_3@\text{SnO}_2(\text{Sn}-0.68)$  dosage has an optimum value for RhB degradation, and when the ratio of  $\text{H}_2\text{O}_2$  concentration to  $\text{Fe}_2\text{O}_3@\text{SnO}_2(\text{Sn}-0.68)$  dosage is around 1 (M): 1 (g/L), e.g.  $0.6 \text{ M}$  of  $\text{H}_2\text{O}_2$  versus  $0.6 \text{ g/L}$  of catalyst (Fig. 9a) and  $0.4 \text{ M}$  of  $\text{H}_2\text{O}_2$  versus  $0.4 \text{ g/L}$  of catalyst (Fig. 9b), RhB degradation will reach higher efficiency. This discovery means that there will be a good cooperation between  $\text{H}_2\text{O}_2$  and catalyst under such a condition, and it may guide a running of photo-Fenton system catalyzed by  $\text{Fe}_2\text{O}_3@\text{SnO}_2(\text{Sn}-0.68)$  with maximum atom economy and minimum negative  $\text{HO}^\bullet$  consumption.

The pH value is a key parameter in Fenton or Fenton-like process that can affect the degradation efficiency of organic pollutants greatly [68]. Although homogeneous Fenton process is generally constrained in acidic conditions, it can be found that the heterogeneous photo-Fenton system catalyzed by  $\text{Fe}_2\text{O}_3@\text{SnO}_2(\text{Sn}-0.68)$  in our case can work for a wider pH range (Fig. 9c). When the initial pH value increase from 3.93 to 7.73, there is a very slight enhancement in the RhB degradation efficiency, even at higher pH value (8.70), over 90% RhB can still be removed in 60 min. This is because there are rather limited free ferric ions in heterogeneous system, and  $\text{Fe}(\text{OH})_3$  with low activity will not be generated. The gradual

increase of initial pH value will facilitate rate-limiting step reaction (Eq. (3)) and generate desirable  $\text{Fe}^{2+}$  sites on the surface of  $\alpha\text{-Fe}_2\text{O}_3$ , which can accelerate the activation of  $\text{H}_2\text{O}_2$  and release more  $\text{HO}^\bullet$ . However, the relatively low redox potential of  $\text{HO}^\bullet$  in neutral and basic media fails to bring an obvious improvement in RhB degradation [82]. When the initial pH is further increased, more  $\text{OH}^-$  will occupy  $\text{Fe}^{3+}$  sites, and thus the interaction between  $\text{Fe}^{3+}$  and  $\text{H}_2\text{O}_2$  (Eq. (3)) will be effectively suppressed, resulting in a lower degradation rate of RhB. Similar phenomena have also been reported in the cases of heterogeneous photo-Fenton process [59,83,84]. Fig. 9d illustrates that a higher reaction temperature only results in a little bit faster RhB degradation. The possible reason for this phenomenon is that higher reaction temperature can lower the reaction activation energy between  $\text{HO}^\bullet$  and organic molecules, while it will also suppress the generation of  $\text{HO}^\bullet$  because Fenton/Fenton-like process is typical exothermic reaction [85]. The catalytic stability of  $\text{Fe}_2\text{O}_3@\text{SnO}_2(\text{Sn}-0.68)$  is also tested. As shown in Fig. S13, no obvious loss of RhB degradation is presented in three consecutive cycles, and quite similar degradation efficiency for each batch experiment demonstrate the excellent catalytic stability of  $\text{Fe}_2\text{O}_3@\text{SnO}_2(\text{Sn}-0.68)$ .

#### 4. Conclusion

$\text{SnO}_2$ -encapsulated  $\alpha\text{-Fe}_2\text{O}_3$  nanocubes have been successfully constructed through an *in situ* transformation of Prussian blue (PB) $@\text{Sn}(\text{OH})\text{Cl}$  nanocubes by high-temperature treatment.  $\text{SnO}_2$  shells play an important role in stabilizing the microstructure of internal  $\text{Fe}_2\text{O}_3$  nanocubes at high-temperature treatment, and meanwhile, they account for an unexpected phase variation from metastable  $\beta$ -/  $\gamma$ -phase to stable  $\alpha$ -phase. The effect of calcination temperature on the microstructure and crystalline phase are also investigated, and the results further confirm the particular contribution of  $\text{SnO}_2$  shells to internal  $\text{Fe}_2\text{O}_3$  in the nanocomposites. Compared with commercial  $\alpha\text{-Fe}_2\text{O}_3$  and PB-derived  $\text{Fe}_2\text{O}_3$ ,

$\text{Fe}_2\text{O}_3@\text{SnO}_2$  nanocubes herein display much better catalytic efficiency in heterogeneous photo-Fenton degradation of Rhodamine B (RhB). The studies of radicals quenching and trapping demonstrate that hydroxyl radical ( $\text{HO}^\bullet$ ) is still the main reactive species, and thus the enhanced catalytic activity is attributed to the stable microstructure and preferable crystalline phase. It is more important that  $\text{Fe}_2\text{O}_3@\text{SnO}_2$  nanocubes can maintain their excellent catalytic efficiency during the repeated batch experiments. These results may provide an exciting clue for the design and fabrication of various high-performance metal oxides derived from metal-organic frameworks in the future.

## Acknowledgements

This work is supported by the financial support from Natural Science Foundation of China (21676065, 21371039, and 21571043), and the Natural Science Foundation of Heilongjiang Province (B201405).

## Appendix A. Supplementary data

Supplementary data associated with this article can be found, in the online version, at <http://dx.doi.org/10.1016/j.apcatb.2017.03.037>.

## References

- [1] A.Y. Hoekstra, Water scarcity challenges to business, *Nat. Clim. Change* 4 (2014) 318–320.
- [2] C.J. Vorosmarty, P.B. McIntyre, M.O. Gessner, D. Dudgeon, A. Prusevich, P. Green, S. Glidden, S.E. Bunn, C.A. Sullivan, C.R. Liermann, P.M. Davies, Global threats to human water security and river biodiversity, *Nature* 467 (2010) 555–561.
- [3] C. Tang, H. Bai, L. Liu, X. Zan, P. Gao, D.D. Sun, W. Yan, A green approach assembled multifunctional Ag/AgBr/TNF membrane for clean water production & disinfection of bacteria through utilizing visible light, *Appl. Catal. B-Environ.* 196 (2016) 57–67.
- [4] R. Li, L. Zhang, P. Wang, Rational design of nanomaterials for water treatment, *Nanoscale* 7 (2015) 17167–17194.
- [5] P.A. Neale, A. Antony, M.E. Bartkow, M.J. Farré, A. Heitz, I. Kristiana, J.Y.M. Tang, B.I. Escher, Bioanalytical assessment of the formation of disinfection byproducts in a drinking water treatment plant, *Environ. Sci. Technol.* 46 (2012) 10317–10325.
- [6] X. Li, C. Bian, X. Meng, F.-S. Xiao, Design and synthesis of an efficient nanoporous adsorbent for  $\text{Hg}^{2+}$  and  $\text{Pb}^{2+}$  ions in water, *J. Mater. Chem. A* 4 (2016) 5999–6005.
- [7] M.A. Shannon, P.W. Bohn, M. Elimelech, J.G. Georgiadis, B.J. Marinas, A.M. Mayes, Science and technology for water purification in the coming decades, *Nature* 452 (2008) 301–310.
- [8] E.I. Unuabonah, C. Günter, J. Weber, S. Lubahn, A. Taubert, Hybrid clay: a new highly efficient adsorbent for water treatment, *ACS Sustain. Chem. Eng.* 1 (2013) 966–973.
- [9] L. Zhang, X. He, X. Xu, C. Liu, Y. Duan, L. Hou, Q. Zhou, C. Ma, X. Yang, R. Liu, F. Yang, L. Cui, C. Xu, Y. Li, Highly active  $\text{TiO}_2/\text{g-C}_3\text{N}_4/\text{G}$  photocatalyst with extended spectral response towards selective reduction of nitrobenzene, *Appl. Catal. B-Environ.* 203 (2017) 1–8.
- [10] M. Li, Z. Qiang, P. Hou, J.R. Bolton, J. Qu, P. Li, C. Wang, VUV/UV/chlorine as an enhanced advanced oxidation process for organic pollutant removal from water: assessment with a novel mini-fluidic VUV/UV photoreaction system (MVPS), *Environ. Sci. Technol.* 50 (2016) 5849–5856.
- [11] J. Giménez, B. Bayarri, Ó. González, S. Malato, J. Peral, S. Espugas, Advanced oxidation processes at laboratory scale: environmental and economic impacts, *ACS Sustain. Chem. Eng.* 3 (2015) 3188–3196.
- [12] Y. Yang, J.J. Pignatello, J. Ma, W.A. Mitch, Comparison of halide impacts on the efficiency of contaminant degradation by sulfate and hydroxyl radical-based advanced oxidation processes (AOPs), *Environ. Sci. Technol.* 48 (2014) 2344–2351.
- [13] X. Xue, K. Hanna, N. Deng, Fenton-like oxidation of Rhodamine B in the presence of two types of iron (II, III) oxide, *J. Hazard. Mater.* 166 (2009) 407–414.
- [14] J. Shi, Z. Ai, L. Zhang, Fe@ $\text{Fe}_2\text{O}_3$  core-shell nanowires enhanced Fenton oxidation by accelerating the  $\text{Fe}(\text{III})/\text{Fe}(\text{II})$  cycles, *Water Res.* 59 (2014) 145–153.
- [15] L. Chen, J. Ma, X. Li, J. Zhang, J. Fang, Y. Guan, P. Xie, Strong enhancement on Fenton oxidation by addition of hydroxylamine to accelerate the ferric and ferrous iron cycles, *Environ. Sci. Technol.* 45 (2011) 3925–3930.
- [16] S. Rahim Pouran, A.R. Abdul Aziz, W.M.A. Wan Daud, Z. Embong, Niobium substituted magnetite as a strong heterogeneous Fenton catalyst for wastewater treatment, *Appl. Surf. Sci.* 351 (2015) 175–187.
- [17] Y. Liu, W. Jin, Y. Zhao, G. Zhang, W. Zhang, Enhanced catalytic degradation of methylene blue by  $\alpha\text{-Fe}_2\text{O}_3/\text{graphene oxide}$  via heterogeneous photo-Fenton reactions, *Appl. Catal. B-Environ.* 206 (2017) 642–652.
- [18] S. Jana, A. Mondal, Fabrication of  $\text{SnO}_2/\alpha\text{-Fe}_2\text{O}_3$ ,  $\text{SnO}_2/\alpha\text{-Fe}_2\text{O}_3\text{-PB}$  heterostructure thin films: enhanced photodegradation and peroxide sensing, *ACS Appl. Mater. Interfaces* 6 (2014) 15832–15840.
- [19] M. Chen, W. Li, X. Shen, G. Diao, Fabrication of core-shell  $\alpha\text{-Fe}_2\text{O}_3@\text{Li}_2\text{Ti}_5\text{O}_{12}$  composite and its application in the lithium ion batteries, *ACS Appl. Mater. Interfaces* 6 (2014) 4514–4523.
- [20] Y. Hou, F. Zuo, A. Dagg, P. Feng, Visible light-driven  $\alpha\text{-Fe}_2\text{O}_3$  nanorod/graphene/BiV<sub>1-x</sub>Mo<sub>x</sub>O<sub>4</sub> core/shell heterojunction array for efficient photoelectrochemical water splitting, *Nano Lett.* 12 (2012) 6464–6473.
- [21] B. Sun, J. Horvat, H.S. Kim, W.-S. Kim, J. Ahn, G. Wang, Synthesis of mesoporous  $\alpha\text{-Fe}_2\text{O}_3$  nanostructures for highly sensitive gas sensors and high capacity anode materials in lithium ion batteries, *J. Phys. Chem. C* 114 (2010) 18753–18761.
- [22] K.-A. Kwon, H.-S. Lim, Y.-K. Sun, K.-D. Suh,  $\alpha\text{-Fe}_2\text{O}_3$  submicron spheres with hollow and macroporous structures as high-performance anode materials for lithium ion batteries, *J. Phys. Chem. C* 118 (2014) 2897–2907.
- [23] B. Wang, J.S. Chen, H.B. Wu, Z. Wang, X.W. Lou, Quasiemulsion-templated formation of  $\alpha\text{-Fe}_2\text{O}_3$  hollow spheres with enhanced lithium storage properties, *J. Am. Chem. Soc.* 133 (2011) 17146–17148.
- [24] F. Jiao, A. Harrison, J.-C. Jumas, A.V. Chadwick, W. Kockelmann, P.G. Bruce, Ordered mesoporous  $\text{Fe}_2\text{O}_3$  with crystalline walls, *J. Am. Chem. Soc.* 128 (2006) 5468–5474.
- [25] Y. Lü, W. Zhan, Y. He, Y. Wang, X. Kong, Q. Kuang, Z. Xie, L. Zheng, MOF-templated synthesis of porous  $\text{Co}_3\text{O}_4$  concave nanocubes with high specific surface area and their gas sensing properties, *ACS Appl. Mater. Interfaces* 6 (2014) 4186–4195.
- [26] X. Zhang, W. Qin, D. Li, D. Yan, B. Hu, Z. Sun, L. Pan, Metal-organic framework derived porous CuO/Cu<sub>2</sub>O composite hollow octahedrons as high performance anode materials for sodium ion batteries, *Chem. Commun.* 51 (2015) 16413–16416.
- [27] S. Chen, M. Xue, Y. Li, Y. Pan, L. Zhu, S. Qiu, Rational design and synthesis of  $\text{Ni}_x\text{Co}_{3x}\text{O}_4$  nanoparticles derived from multivariate MOF-74 for supercapacitors, *J. Mater. Chem. A* 3 (2015) 20145–20152.
- [28] Y. Kimitsuka, E. Hosono, S. Ueno, H. Zhou, S. Fujihara, Fabrication of porous cubic architecture of ZnO using Zn-terephthalate MOFs with characteristic microstructures, *Inorg. Chem.* 52 (2013) 14028–14033.
- [29] R.R. Salunkhe, J. Tang, Y. Kamachi, T. Nakato, J.H. Kim, Y. Yamauchi, Asymmetric supercapacitors using 3D nanoporous carbon and cobalt oxide electrodes synthesized from a single metal-organic framework, *ACS Nano* 9 (2015) 6288–6296.
- [30] L. Peng, J. Zhang, Z. Xue, B. Han, J. Li, G. Yang, Large-pore mesoporous  $\text{Mn}_3\text{O}_4$  crystals derived from metal-organic frameworks, *Chem. Commun.* 49 (2013) 11695–11697.
- [31] K.E. deKrafft, C. Wang, W. Lin, Metal-organic framework templated synthesis of  $\text{Fe}_2\text{O}_3/\text{TiO}_2$  nanocomposite for hydrogen production, *Adv. Mater.* 24 (2012) 2014–2018.
- [32] L. Zhang, H.B. Wu, S. Madhavi, H.H. Hng, X.W. Lou, Formation of  $\text{Fe}_2\text{O}_3$  microboxes with hierarchical shell structures from metal-organic frameworks and their lithium storage properties, *J. Am. Chem. Soc.* 134 (2012) 17388–17391.
- [33] M. Hu, J.-S. Jiang, Y. Zeng, Prussian blue microcrystals prepared by selective etching and their conversion to mesoporous magnetic iron(III) oxides, *Chem. Commun.* 46 (2010) 1133–1135.
- [34] S. Sakurai, A. Namai, K. Hashimoto, S.-I. Ohkoshi, First observation of phase transformation of all four  $\text{Fe}_2\text{O}_3$  phases ( $\gamma \rightarrow \varepsilon \rightarrow \beta \rightarrow \alpha$ -Phase), *J. Am. Chem. Soc.* 131 (2009) 18299–18303.
- [35] M. Zhang, W. Pu, S. Pan, O.K. Okoth, C. Yang, J. Zhang, Photoelectrocatalytic activity of liquid phase deposited  $\alpha\text{-Fe}_2\text{O}_3$  films under visible light illumination, *J. Alloys Compd.* 648 (2015) 719–725.
- [36] M. Caggioni, J. Lenis, A.V. Bayles, E.M. Furst, P.T. Spicer, Temperature-induced collapse, and arrested collapse of anisotropic endoskeleton droplets, *Langmuir* 31 (2015) 8558–8565.
- [37] M. Aznaryan, D. Nettels, A. Holla, H. Hofmann, B. Schuler, Single-molecule spectroscopy of cold denaturation and the temperature-induced collapse of unfolded proteins, *J. Am. Chem. Soc.* 135 (2013) 14040–14043.
- [38] G.K. Pradhan, K.H. Reddy, K.M. Parida, Facile fabrication of mesoporous  $\alpha\text{-Fe}_2\text{O}_3/\text{SnO}_2$  nanoheterostructure for photocatalytic degradation of malachite green, *Catal. Today* 224 (2014) 171–179.
- [39] G. Yue, H. Ni, R. Chen, Z. Wang, C. Zhang, W. Zhan, Y. Li, J. Li, Efficient growth of aligned  $\text{SnO}_2$  nanorod arrays on hematite ( $\alpha\text{-Fe}_2\text{O}_3$ ) nanotube arrays for photoelectrochemical and photocatalytic applications, *J. Mater. Sci.-Mater. Electron.* 24 (2013) 3324–3329.
- [40] Z. Yang, H. Wang, W. Song, W. Wei, Q. Mu, B. Kong, P. Li, H. Yin, One dimensional  $\text{SnO}_2$  NRs/ $\text{Fe}_2\text{O}_3$  NTs with dual synergistic effects for photoelectrocatalytic reduction  $\text{CO}_2$  into methanol, *J. Colloid Interface Sci.* 486 (2017) 232–240.
- [41] J. Kang, Q. Kuang, Z.-X. Xie, L.-S. Zheng, Fabrication of the  $\text{SnO}_2/\alpha\text{-Fe}_2\text{O}_3$  hierarchical heterostructure and its enhanced photocatalytic property, *J. Phys. Chem. C* 115 (2011) 7874–7879.

- [42] Y. Mi, Y.H. Cao, X.L. Liu, J.B. Yi, H.R. Tan, P. Ma, H. Hao, X. Zhang, H.M. Fan, Synthesis of hierarchical  $\text{Fe}_2\text{O}_3/\text{SnO}_2$  hollow heterostructures and their improved photocatalytic properties, *Mater. Chem. Phys.* 143 (2013) 311–321.
- [43] K. Yu, Z. Wu, Q. Zhao, B. Li, Y. Xie, High-temperature-stable  $\text{Au@SnO}_2$  core/shell supported catalyst for CO oxidation, *J. Phys. Chem. C* 112 (2008) 2244–2247.
- [44] S.H. Lee, D.M. Hoffman, A.J. Jacobson, T.R. Lee, Transparent, homogeneous tin Oxide ( $\text{SnO}_2$ ) thin films containing  $\text{SnO}_2$ -coated gold nanoparticles, *Chem. Mater.* 25 (2013) 4697–4702.
- [45] L. Wang, Z. Lou, R. Zhang, T. Zhou, J. Deng, T. Zhang, Hybrid  $\text{Co}_3\text{O}_4/\text{SnO}_2$  core-shell nanospheres as real-time rapid-response sensors for ammonia gas, *ACS Appl. Mater. Interfaces* 8 (2016) 6539–6545.
- [46] Y. Cao, T. He, L. Zhao, E. Wang, W. Yang, Y. Cao, Structure and phase transition behavior of  $\text{Sn}^{4+}$ -doped  $\text{TiO}_2$  nanoparticles, *J. Phys. Chem. C* 113 (2009) 18121–18124.
- [47] F. Wang, J.H. Ho, Y. Jiang, R. Amal, Tuning phase composition of  $\text{TiO}_2$  by  $\text{Sn}^{4+}$  doping for efficient photocatalytic hydrogen generation, *ACS Appl. Mater. Interfaces* 7 (2015) 23941–23948.
- [48] R. Qiang, Y. Du, H. Zhao, Y. Wang, C. Tian, Z. Li, X. Han, P. Xu, Metal organic framework-derived Fe/C nanocubes toward efficient microwave absorption, *J. Mater. Chem. A* 3 (2015) 13426–13434.
- [49] Y. Du, S. Liu, Y. Ji, Y. Zhang, S. Wei, F. Liu, F.-S. Xiao, Synthesis of sulfated silica-doped tin oxides and their high activities in transesterification, *Catal. Lett.* 124 (2008) 133–138.
- [50] H.-M. Jeong, J.-H. Kim, S.-Y. Jeong, C.-H. Kwak, J.-H. Lee,  $\text{Co}_3\text{O}_4-\text{SnO}_2$  hollow heteronanostructures: facile control of gas selectivity by compositional tuning of sensing materials via galvanic replacement, *ACS Appl. Mater. Interfaces* 8 (2016) 7877–7883.
- [51] C. Karunakaran, S. SakthiRaadha, P. Gomathisankar, Photocatalytic and bactericidal activities of hydrothermally and sonochemically prepared  $\text{Fe}_2\text{O}_3-\text{SnO}_2$  nanoparticles, *Mater. Sci. Semicond. Process* 16 (2013) 818–824.
- [52] Y.P. He, Y.M. Miao, C.R. Li, S.Q. Wang, L. Cao, S.S. Xie, G.Z. Yang, B.S. Zou, C. Burda, Size and structure effect on optical transitions of iron oxide nanocrystals, *Phys. Rev. B* 71 (2005) 125411.
- [53] Q. Tian, W. Wu, L. Sun, S. Yang, M. Lei, J. Zhou, Y. Liu, X. Xiao, F. Ren, C. Jiang, V.A.L. Roy, Tube-like ternary  $\alpha\text{-Fe}_2\text{O}_3@\text{SnO}_2@\text{Cu}_2\text{O}$  sandwich heterostructures: synthesis and enhanced photocatalytic properties, *ACS Appl. Mater. Interfaces* 6 (2014) 13088–13097.
- [54] K.S. Walton, R.Q. Snurr, Applicability of the BET method for determining surface areas of microporous metal-organic frameworks, *J. Am. Chem. Soc.* 129 (2007) 8552–8556.
- [55] S. Blacher, R. Pirard, J.P. Pirard, B. Sahouli, F. Brouers, On the texture characterization of mixed  $\text{SiO}_2-\text{ZrO}_2$  aerogels using the nitrogen adsorption-desorption isotherms: classical and fractal methods, *Langmuir* 13 (1997) 1145–1149.
- [56] G. Amarasekera, M.J. Scarlett, D.E. Mainwaring, High-resolution adsorption isotherms of microporous solids, *J. Phys. Chem. C* 100 (1996) 7580–7585.
- [57] W. Li, Y. Wang, A. Irini, Effect of pH and  $\text{H}_2\text{O}_2$  dosage on catechol oxidation in nano- $\text{Fe}_3\text{O}_4$  catalyzing UV-Fenton and identification of reactive oxygen species, *Chem. Eng. J.* 244 (2014) 1–8.
- [58] F. Chai, K. Li, C. Song, X. Guo, Synthesis of magnetic porous  $\text{Fe}_3\text{O}_4/\text{C}/\text{Cu}_2\text{O}$  composite as an excellent photo-Fenton catalyst under neutral condition, *J. Colloid Interface Sci.* 475 (2016) 119–125.
- [59] B. Qiu, Q. Li, B. Shen, M. Xing, J. Zhang, Stöber-like method to synthesize ultradispersed  $\text{Fe}_3\text{O}_4$  nanoparticles on graphene with excellent photo-Fenton reaction and high-performance lithium storage, *Appl. Catal. B-Environ.* 183 (2016) 216–223.
- [60] L. Xu, J. Wang, Magnetic nanoscaled  $\text{Fe}_3\text{O}_4/\text{CeO}_2$  composite as an efficient Fenton-like heterogeneous catalyst for degradation of 4-chlorophenol, *Environ. Sci. Technol.* 46 (2012) 10145–10153.
- [61] C. Zhu, Y. Li, Q. Su, B. Lu, J. Pan, J. Zhang, E. Xie, W. Lan, Electrospinning direct preparation of  $\text{SnO}_2/\text{Fe}_2\text{O}_3$  heterojunction nanotubes as an efficient visible-light photocatalyst, *J. Alloys Compd.* 575 (2013) 333–338.
- [62] H. Xia, H. Zhuang, T. Zhang, D. Xiao, Visible-light-activated nanocomposite photocatalyst of  $\text{Fe}_2\text{O}_3/\text{SnO}_2$ , *Mater. Lett.* 62 (2008) 1126–1128.
- [63] X. Li, Y. Pi, L. Wu, Q. Xia, J. Wu, Z. Li, J. Xiao, Facilitation of the visible light-induced Fenton-like excitation of  $\text{H}_2\text{O}_2$  via heterojunction of g-C<sub>3</sub>N<sub>4</sub>/NH<sub>2</sub>-iron terephthalate metal-organic framework for MB degradation, *Appl. Catal. B-Environ.* 202 (2017) 653–663.
- [64] Y. Zhang, J. Gu, M. Muruganathan, Y. Zhang, Development of novel  $\alpha\text{-Fe}_2\text{O}_3/\text{NiTiO}_3$  heterojunction nanofibers material with enhanced visible-light photocatalytic performance, *J. Alloys Compd.* 630 (2015) 110–116.
- [65] X. Li, J. Liu, A.I. Rykov, H. Han, C. Jin, X. Liu, J. Wang, Excellent photo-Fenton catalysts of Fe-Co Prussian blue analogues and their reaction mechanism study, *Appl. Catal. B-Environ.* 179 (2015) 196–205.
- [66] X. Chen, F. Chen, F. Liu, X. Yan, W. Hu, G. Zhang, L. Tian, Q. Xi, X. Chen, Ag nanoparticles/hematite mesocrystals superstructure composite: a facile synthesis and enhanced heterogeneous photo-Fenton activity, *Catal. Sci. Technol.* 6 (2016) 4184–4191.
- [67] L. Tian, K. Deng, L. Ye, L. Zan, Effect of surface ethoxy groups on photoactivity of  $\text{TiO}_2$  nanocrystals, *Appl. Surf. Sci.* 257 (2011) 10653–10658.
- [68] E. Neyens, J. Baeyens, A review of classic Fenton's peroxidation as an advanced oxidation technique, *J. Hazard. Mater.* 98 (2003) 33–50.
- [69] T. Jiang, A.S. Poyraz, A. Iyer, Y. Zhang, Z. Luo, W. Zhong, R. Miao, A.M. El-Sawy, C.J. Guild, Y. Sun, D.A. Kriz, S.L. Suib, Synthesis of mesoporous iron oxides by an inverse micelle method and their application in the degradation of orange II under visible light at neutral pH, *J. Phys. Chem. C* 119 (2015) 10454–10468.
- [70] S. Shuang, R. Lv, Z. Xie, W. Wang, X. Cui, S. Ning, Z. Zhang,  $\alpha\text{-Fe}_2\text{O}_3$  nanopillar arrays fabricated by electron beam evaporation for the photoassisted degradation of dyes with  $\text{H}_2\text{O}_2$ , *RSC Adv.* 6 (2016) 534–540.
- [71] X. Wang, J. Wang, Z. Cui, S. Wang, M. Cao, Facet effect of  $\alpha\text{-Fe}_2\text{O}_3$  crystals on photocatalytic performance in the photo-Fenton reaction, *RSC Adv.* 4 (2014) 34387–34394.
- [72] L. Gu, J. Wang, H. Cheng, Y. Zhao, L. Liu, X. Han, One-step preparation of graphene-supported anatase  $\text{TiO}_2$  with exposed {001} facets and mechanism of enhanced photocatalytic properties, *ACS Appl. Mater. Interfaces* 5 (2013) 3085–3093.
- [73] Z. Cheng, H. Zhou, J. Yin, L. Yu, Electron spin resonance estimation of hydroxyl radical scavenging capacity for lipophilic antioxidants, *J. Agric. Food Chem.* 55 (2007) 3325–3333.
- [74] F. Xu, X.-N. Song, G.-P. Sheng, H.-W. Luo, W.-W. Li, R.-S. Yao, H.-Q. Yu, Vitamin B<sub>2</sub>-initiated hydroxyl radical generation under visible light in the presence of dissolved iron, *ACS Sustain. Chem. Eng.* 3 (2015) 1756–1763.
- [75] D.-F. Zhang, L.-D. Sun, C.-J. Jia, Z.-G. Yan, L.-P. You, C.-H. Yan, Hierarchical assembly of  $\text{SnO}_2$  nanorod arrays on  $\alpha\text{-Fe}_2\text{O}_3$  nanotubes: a case of interfacial lattice compatibility, *J. Am. Chem. Soc.* 127 (2005) 13492–13493.
- [76] W. Wu, S. Zhang, F. Ren, X. Xiao, J. Zhou, C. Jiang, Controlled synthesis of magnetic iron oxides@ $\text{SnO}_2$  quasi-hollow core-shell heterostructures: formation mechanism, and enhanced photocatalytic activity, *Nanoscale* 3 (2011) 4676–4684.
- [77] Q. Zhai, L. Zhang, X. Zhao, H. Chen, D. Yin, J. Li, A novel iron-containing polyoxometalate heterogeneous photocatalyst for efficient 4-chlorophenol degradation by  $\text{H}_2\text{O}_2$  at neutral pH, *Appl. Surf. Sci.* 377 (2016) 17–22.
- [78] Z. Huang, P. Wu, B. Gong, S. Yang, H. Li, Z. Zhu, L. Cui, Preservation of glutamic acid-iron chelate into montmorillonite to efficiently degrade reactive blue 19 in a Fenton system under sunlight irradiation at neutral pH, *Appl. Surf. Sci.* 370 (2016) 209–217.
- [79] W. Najjar, S. Azabou, S. Sayadi, A. Ghorbel, Catalytic wet peroxide photo-oxidation of phenolic olive oil mill wastewater contaminants: part I. Reactivity of tyrosol over (Al-Fe)PILC, *Appl. Catal. B-Environ.* 74 (2007) 11–18.
- [80] Z. Wang, Y. Du, Y. Liu, B. Zou, J. Xiao, J. Ma, Degradation of organic pollutants by  $\text{NiFe}_2\text{O}_4/\text{peroxymonosulfate}$ : efficiency, influential factors and catalytic mechanism, *RSC Adv.* 6 (2016) 11040–11048.
- [81] Y. Du, W. Ma, P. Liu, B. Zou, J. Ma, Magnetic  $\text{CoFe}_2\text{O}_4$  nanoparticles supported on titanate nanotubes ( $\text{CoFe}_2\text{O}_4/\text{TNTs}$ ) as a novel heterogeneous catalyst for peroxymonosulfate activation and degradation of organic pollutants, *J. Hazard. Mater.* 308 (2016) 58–66.
- [82] J. Du, J. Bao, X. Fu, C. Lu, S.H. Kim, Mesoporous sulfur-modified iron oxide as an effective Fenton-like catalyst for degradation of bisphenol A, *Appl. Catal. B-Environ.* 184 (2016) 132–141.
- [83] G.M.S. ElShafei, F.Z. Yehia, O.I.H. Dimitry, A.M. Badawi, G. Eshaq, Extending the working pH of nitrobenzene degradation using ultrasonic/heterogeneous Fenton to the alkaline range via amino acid modification, *Chemosphere* 139 (2015) 632–637.
- [84] S. Guo, G. Zhang, Y. Guo, J.C. Yu, Graphene oxide- $\text{Fe}_2\text{O}_3$  hybrid material as highly efficient heterogeneous catalyst for degradation of organic contaminants, *Carbon* 60 (2013) 437–444.
- [85] M. Cheng, G. Zeng, D. Huang, C. Lai, P. Xu, C. Zhang, Y. Liu, J. Wan, X. Gong, Y. Zhu, Degradation of atrazine by a novel Fenton-like process and assessment the influence on the treated soil, *J. Hazard. Mater.* 312 (2016) 184–191.